

## SUBMILLIMETER ARRAY AND VERY LARGE ARRAY OBSERVATIONS IN THE HYPERCOMPACT H II REGION G35.58-0.03

CHUAN-PENG ZHANG<sup>1,2,3,4</sup>, JUN-JIE WANG<sup>1,3</sup>, JIN-LONG XU<sup>1,3</sup>, FRIEDRICH WYROWSKI<sup>2</sup>, KARL M. MENTEN<sup>2</sup>  
*Draft version February 28, 2024*

### ABSTRACT

The formation of hypercompact (HC) H II regions is an important stage in massive star formation. Spectral line and continuum observations can explore its dynamic conditions. We present high angular resolution observations carried out with the Submillimeter Array (SMA) and the Very Large Array (VLA) toward the HC H II region G35.58-0.03. With the 1.3 mm SMA and 1.3 cm VLA, we detected a total of about 25 transitions of 8 different species and their isotopologues (CO, CH<sub>3</sub>CN, SO<sub>2</sub>, CH<sub>3</sub>CCH, OCS, CS, H, and NH<sub>3</sub>). G35.58-0.03 consists of an HC H II core with electron temperature  $T_e^* \geq 5500$  K, emission measure  $EM \approx 1.9 \times 10^9$  pc cm<sup>-6</sup>, local volume electron density  $n_e = 3.3 \times 10^5$  cm<sup>-3</sup>, and a same width of radio recombination line FWHM  $\approx 43.2$  km s<sup>-1</sup> for both H30 $\alpha$  and H38 $\beta$  at its intrinsic core size  $\sim 3714$  AU. The H30 $\alpha$  line shows evidence of an ionized outflow driving a molecular outflow. Based on the derived Lyman continuum flux, there should be an early-type star equivalent to O6.5 located inside the H II region. From the continuum spectral energy distribution from 3.6 cm, 2.0 cm, 1.3 cm, 1.3 mm and 0.85 mm to 0.45 mm, we distinguished the free-free emission (25%  $\sim$  55%) from the warm dust component (75%  $\sim$  45%) at 1.3 mm. The molecular envelope shows evidence of infall and outflow with an infall rate  $0.05 M_\odot$  yr<sup>-1</sup> and a mass loss rate  $5.2 \times 10^{-3} M_\odot$  yr<sup>-1</sup>. The derived momentum ( $\sim 0.05 M_\odot$  km s<sup>-1</sup>) is consistent between the infalling and outflowing gas per year. It is suggested that the infall is predominant and the envelope mass of dense core is increasing rapidly, but the accretion in the inner part might already be halted.

*Subject headings:* H II regions — ISM: individual (G35.58-0.03) — stars: formation

### 1. INTRODUCTION

Massive star formation ( $\gtrsim 10 M_\odot$ ) is difficult to understand because of the large distance ( $\gtrsim 1$  kpc), high extinction ( $A_V \gtrsim 100$  mag), and short evolutionary timescale ( $\lesssim 10^4$  yr) (Kurtz 2005; van der Tak & Menten 2005) of massive star formation regions. High angular resolution millimeter observations are able to unveil the physical envelope conditions of individual cores. High angular resolution centimeter observations can penetrate the dense dust emission of cores to search for hypercompact (HC) H II or ultracompact (UC) H II regions excited by the embedded protostar.

HC H II regions are associated with the earliest stages that the central object has a mass equivalent to an O star. Early B- and O-type stars are usually found to be deeply embedded in dense molecular clouds where they produce HC H II or UC H II regions. The HC H II regions often show roughly linear continuum spectral energy distributions (SEDs) with frequency  $S_\nu \propto \nu^\alpha$  in the region up to  $\sim 100$  GHz (Franco et al. 2000; Beuther et al. 2004; Keto et al. 2008; Galván-Madrid et al. 2009). The variation of index  $\alpha$  can trace the density gradients in the ionized gas (Franco et al. 2000). Typically HC H II regions have small size ( $\lesssim 0.03$  pc), high elec-

tron density ( $10^5 - 10^6$  cm<sup>-3</sup>), high emission measure ( $\gtrsim 10^8$  pc cm<sup>-6</sup>), very broad radio recombination lines (FWHM  $\gtrsim 40$  km s<sup>-1</sup>) (Kurtz 2000; Beuther et al. 2007; Sewilo et al. 2011; Choi et al. 2012). HC H II regions are usually more advanced in evolution than hot molecular cores and younger than UC H II regions (Kurtz 2000). However, there are some HC H II regions (presumably those where the central stars are still accreting) where the HC H II region coexists with a hot core. HC H II regions will evolve into UC H II regions with expanding their size. Unveiling the evolution process of HC H II regions is helpful to understand massive star formation. However, few HC H II regions are known to investigate the evolutionary process of massive star formation.

Usually, the massive star formation process is accompanied by infall, outflow, and/or rotation movements. Infall and accretion increase the mass of massive stars. Outflows transfer angular momentum of infalling gas (Keto 2002, 2007). High angular resolution Submillimeter Array (SMA) and Very Large Array (VLA) observation in millimeter and centimeter wavelength will help to further understand these dynamical phenomena.

The HC H II region G35.58-0.03 is located at the far kinematic distance of 10.2 kpc (Fish et al. 2003; Watson et al. 2003). Water and OH masers (Forster & Caswell 1989; De Buizer et al. 2005; Fish et al. 2005), but no methanol masers (Caswell et al. 1995), have been detected at this site. VLA 2 and 3.6 cm maps indicate that G35.58-0.03 is just resolved into two extremely close UC H II regions: western G35.578-0.030 and eastern G35.578-0.031 (Kurtz et al. 1994). The low resolution 3.6 and 21 cm maps show that both G35.578-0.030 and G35.578-0.031 are lying within

cpzhang@mpifr-bonn.mpg.de

<sup>1</sup> National Astronomical Observatories, Chinese Academy of Sciences, 100012 Beijing, China

<sup>2</sup> Max-Planck-Institut für Radioastronomie, Auf dem Hügel 69, D-53121 Bonn, Germany

<sup>3</sup> NAOC-TU Joint Center for Astrophysics, 850000 Lhasa, China

<sup>4</sup> University of the Chinese Academy of Sciences, 100080 Beijing, China

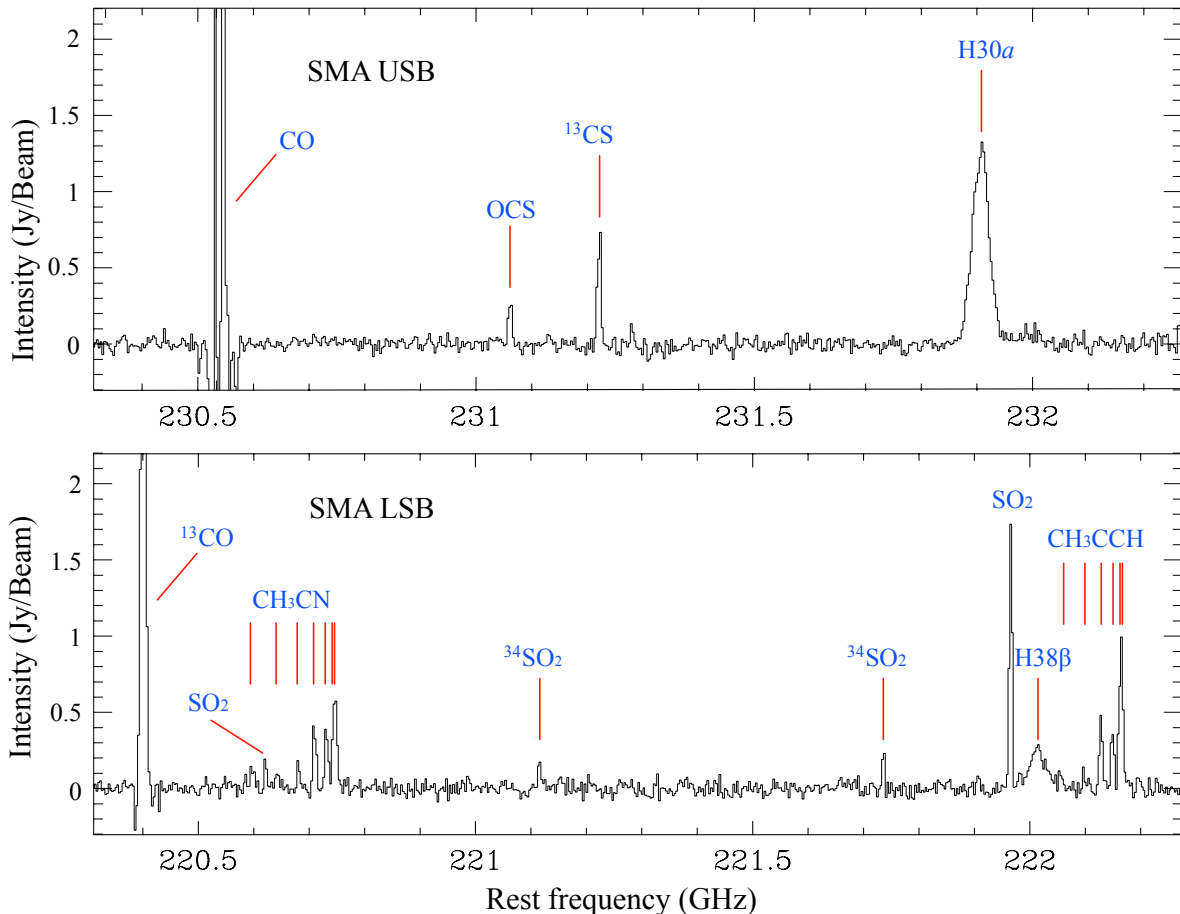


FIG. 1.— Wide-band SMA spectra extracted from the line data-cubes in the image domain at the position of the 1.3 mm continuum peak. The channel spacing in this plot is  $4.25 \text{ km s}^{-1}$ .

large-scale extended continuum emission (Kurtz et al. 1999; De Buizer et al. 2005). In addition, Plume et al. (1992), Mueller et al. (2002), Shirley et al. (2003), and Zhang & Wang (2013) have investigated G35.58-0.03 with low angular resolution, but they did not present its dynamical information, even not to resolve it.

In this work we mainly report on 1.3 millimeter (mm) and 1.3 centimeter (cm) interferometric observations performed with the SMA and the VLA at angular resolutions of  $\sim 3''.4$  and  $\sim 0''.3$ , respectively, toward HC H II region G35.58-0.03. In Section 2, we describe the observations and reduction of archival SMA 1.3 mm and VLA 1.3+3.6 cm data. We present the main results from observations of spectral lines, moments maps, and position-velocity (PV) diagrams in Section 3. In Section 4, we exhibit and discuss some results concerning the physical and dynamical conditions of the HC H II region. Finally, conclusions are given in Section 5.

## 2. OBSERVATIONS AND DATA

### 2.1. SMA

The 1.3 mm data for G35.58-0.03 are publicly available in the SMA data archive<sup>5</sup> (Ho et al. 2004), and

<sup>5</sup> <http://cfa-www.harvard.edu/rtdc/index-sma.html>

were observed on 2008 June 22 in its compact configuration<sup>6</sup>. Two sidebands covered the frequency ranges of 220.3 – 222.3 GHz and 230.3 – 232.3 GHz with a frequency resolution of  $\approx 0.812 \text{ MHz}$  (or velocity resolution of  $0.85 \text{ km s}^{-1}$ ). The approximate synthesized beam size (full width at half-power) is  $3''.53 \times 3''.19$  with position angle (P.A.) =  $76^\circ.3$  for lower sideband, and  $3''.38 \times 3''.05$  with P.A. =  $76^\circ.1$  for upper sideband. The SMA primary beam at 230 GHz is  $\sim 55''$ . The relevant degrees per flux unit factor is  $\text{DPFU}_{1.3 \text{ mm}} \sim 2.22 \text{ K per Jy beam}^{-1}$ .

The phase tracking center was  $\alpha(\text{J2000}) = 18^{\text{h}}56^{\text{m}}22^{\text{s}}.533$  and  $\delta(\text{J2000}) = 02^\circ20'27''.50$ . QSO 3C279 and Uranus were used as bandpass and flux calibrators. QSO J1751+096 and QSO J1830+063 were observed for the antenna gain corrections. The calibration and imaging were performed in Miriad<sup>7</sup>. We summed up the line-free channels, and produced a “pseudo” continuum database that was subtracted from the  $uv$ -database in the  $uv$ -plane. The line-free continuum was self-calibrated, and the gain solutions were applied to the spectral line data. The image data

<sup>6</sup> The SMA is a joint project between the Smithsonian Astrophysical Observatory and the Academia Sinica Institute of Astronomy and Astrophysics and is funded by the Smithsonian Institution and the Academia Sinica.

<sup>7</sup> <http://sma-www.cfa.harvard.edu/miriad>

TABLE 1  
 LINE PARAMETERS AND GAUSSIAN FITTING RESULTS<sup>a b</sup>

Molecule	Transition	Frequency GHz	Flux Jy/beam-km/s	Velocity km/s	FWHM km/s	Intensity Jy/beam
(1)	(2)	(3)	(4)	(5)	(6)	(7)
NH <sub>3</sub>	(2, 2)	23.722633	-0.02(0.01)	47.44(0.58)	2.92(1.47)	-0.007(0.001)
NH <sub>3</sub>	(2, 2)	23.722633	-0.16(0.01)	52.60(0.17)	4.61(0.43)	-0.033(0.001)
NH <sub>3</sub>	(3, 3)	23.870129	-0.04(0.03)	48.17(2.26)	5.24(3.32)	-0.008(0.006)
NH <sub>3</sub>	(3, 3)	23.870129	-0.12(0.04)	53.17(0.35)	4.35(0.64)	-0.026(0.006)
<sup>13</sup> CO	2-1	220.39868	183.90(2.19)	52.19(0.02)	8.39(0.05)	20.60(0.37)
CH <sub>3</sub> CN	12 <sub>6</sub> -11 <sub>6</sub>	220.59444	—	—	—	—
SO <sub>2</sub>	56 <sub>5,51</sub> -57 <sub>4,54</sub>	220.61850	18.47(0.58)	52.21(0.05)	6.21(0.17)	2.79(0.09)
CH <sub>3</sub> CN	12 <sub>5</sub> -11 <sub>5</sub>	220.64110	—	—	—	—
CH <sub>3</sub> CN	12 <sub>4</sub> -11 <sub>4</sub>	220.67930	2.28(0.49)	122.80(0.50)	6.62(1.22)	0.32(0.06)
CH <sub>3</sub> CN	12 <sub>3</sub> -11 <sub>3</sub>	220.70902	5.99(0.44)	82.43(0.22)	8.01(0.53)	0.70(0.06)
CH <sub>3</sub> CN	12 <sub>2</sub> -11 <sub>2</sub>	220.73027	4.91(0.35)	53.41(0.24)	8.19(0.76)	0.56(0.06)
CH <sub>3</sub> CN	12 <sub>1</sub> -11 <sub>1</sub>	220.74302	—	—	—	—
CH <sub>3</sub> CN	12 <sub>0</sub> -11 <sub>0</sub>	220.74727	—	—	—	—
<sup>34</sup> SO <sub>2</sub>	22 <sub>2,20</sub> -22 <sub>1,21</sub>	221.11490	2.81(0.72)	52.56(0.38)	5.66(1.01)	0.47(0.06)
<sup>34</sup> SO <sub>2</sub>	13 <sub>2,12</sub> -13 <sub>1,13</sub>	221.73571	2.53(0.32)	53.02(0.23)	5.30(0.66)	0.45(0.04)
SO <sub>2</sub>	11 <sub>1,11</sub> -10 <sub>0,10</sub>	221.96520	—	—	—	—
H	38β	222.01175	12.11(0.69)	49.87(1.16)	43.18(3.05)	0.26(0.04)
CH <sub>3</sub> CCH	13 <sub>5</sub> -12 <sub>5</sub>	222.06103	—	—	—	—
CH <sub>3</sub> CCH	13 <sub>4</sub> -12 <sub>4</sub>	222.09915	0.95(0.33)	123.00(0.75)	3.99(1.11)	0.22(0.08)
CH <sub>3</sub> CCH	13 <sub>3</sub> -12 <sub>3</sub>	222.12881	5.64(0.38)	81.93(0.11)	7.44(0.60)	0.71(0.08)
CH <sub>3</sub> CCH	13 <sub>2</sub> -12 <sub>2</sub>	222.15001	4.94(0.37)	53.84(0.01)	6.55(0.10)	0.71(0.08)
CH <sub>3</sub> CCH	13 <sub>1</sub> -12 <sub>1</sub>	222.16273	—	—	—	—
CH <sub>3</sub> CCH	13 <sub>0</sub> -12 <sub>0</sub>	222.16697	—	—	—	—
CO	2-1	230.53800	284.60(1.78)	52.86(0.02)	13.53(0.05)	19.80(0.51)
OCS	19-18	231.06099	5.94(1.46)	53.20(0.20)	6.49(0.75)	0.86(0.04)
<sup>13</sup> CS	5-4	231.22077	14.27(1.28)	52.52(0.11)	6.88(0.40)	1.95(0.05)
H	30α	231.90090	61.37(0.68)	45.03(0.23)	43.16(0.42)	1.34(0.05)

<sup>a</sup> All lines are indicated in Figure 1. The Gaussian fitting lines are exhibited in Figures 2 and 4.

<sup>b</sup> The DPFU is  $\sim 2.55 \times 10^4$  K per Jy beam<sup>-1</sup> for VLA data, and  $\sim 2.22$  K per Jy beam<sup>-1</sup> for SMA data.

cubes were exported to CLASS in GILDAS<sup>8</sup> for further spectral line processing. The continuum-free spectra across the entire sidebands at the position of 1.3 mm peak are shown in Figure 1. The rms noise in the final images is in the range of [40, 80] mJy beam<sup>-1</sup> for the line data and  $\sim 19$  mJy beam<sup>-1</sup> for the continuum data.

## 2.2. VLA

The 1.3 cm data for G35.58-0.03 were retrieved from the NRAO<sup>9</sup> VLA archival database. The project code is AG811. The 1.3 cm spectral line observations (NH<sub>3</sub> ( $J, K$ ) = (2, 2) and (3, 3)) are observed in the VLA-B configuration on 2009 March. The phase tracking center was  $\alpha(\text{J2000}) = 18^{\text{h}}56^{\text{m}}22^{\text{s}}500$  and  $\delta(\text{J2000}) = 02^{\circ}20'27''.00$ . The NH<sub>3</sub> ( $J, K$ ) = (2, 2) and (3, 3) inversion transitions were observed simultaneously, using the 2-IF spectral line mode of the correlator, with 6.25 MHz bandwidth and 127 channels of 49 kHz (0.617 km s<sup>-1</sup>) each. The approximate synthesized beam size (full width at half-power) is about  $0''.36 \times 0''.24$  with P.A. = 12°6. The VLA primary beam at 23 GHz is  $\sim 120''$ . The corresponding degrees per flux unit factor is  $\text{DPFU}_{1.3 \text{ cm}} \sim 2.5 \times 10^4$  K per Jy beam<sup>-1</sup>. For calibrations, J1331+305 was used for flux calibrators, J2253+161 and J1331+305

were used for the bandpass, and J18517+00355 was observed for the antenna gain and phase corrections. The flux-density scale was bootstrapped from J1331+305 model assuming a flux-density of 2.4059 Jy for 23.72 GHz and 2.3949 Jy for 23.87 GHz. And the phase calibrator J18517+00355 has a flux-density of  $1.0335 \pm 0.0003$  for 23.72 GHz and  $0.8688 \pm 0.0004$  for 23.87 GHz. The rms noise in the final images is in the range of [1, 6] mJy beam<sup>-1</sup> for the line data and  $\sim 0.7$  mJy beam<sup>-1</sup> for the continuum data.

In addition, the 3.6 cm continuum data were taken from the VLA archive and observed on 1998 December with the VLA-C configuration (project code AK477). The phase tracking center was  $\alpha(\text{J2000}) = 18^{\text{h}}56^{\text{m}}23^{\text{s}}473$  and  $\delta(\text{J2000}) = 02^{\circ}20'37''.76$ . A bandwidth 50 MHz was used and centered at 8.4351 (IF1) and 8.4851 (IF2) GHz each. QSO B1328+307 was used as flux calibrator and QSO B1829-106 was used for gain correction. The rms noise in the final images is  $\sim 6.7$  mJy beam<sup>-1</sup> for the 3.6 cm continuum data.

All VLA data sets were calibrated using standard procedures in the AIPS software<sup>10</sup>. The 1.3 cm continuum was constructed in the ( $u, v$ ) domain from line-free channels and was then self-calibrated. The gain solutions from self-calibration were applied to the line data. The calibrated data were exported to GILDAS and MIRIAD for further processing and imaging.

## 3. OBSERVATIONAL RESULTS

<sup>8</sup> <http://www.iram.fr/IRAMFR/GILDAS/>

<sup>9</sup> The National Radio Astronomy Observatory is operated by Associated Universities, Inc., under cooperative agreement with the National Science Foundation.

<sup>10</sup> <http://www.aips.nrao.edu/index.shtml>

TABLE 2  
CONTINUUM EMISSION OF DIFFERENT WAVELENGTH

Continuum	Right Ascension	Declination	Beam Size	Deconvolved Size	Peak	Total Flux
(1)	h m s (")	° ' " (")	"×"; °	"×"; °	Jy/beam	Jy
	(2)	(3)	(4)	(5)	(6)	(7)
3.6 cm <sup>a</sup>	18 56 22.563(0.05)	2 20 27.660(0.06)	2.82×2.38;-12.5	1.96×1.35;55.1	0.163(0.007)	0.234(0.004)
3.6 cm <sup>b</sup>	18 56 22.52	2 20 27.0	1.05×0.79	—	0.074(0.000)	0.197(0.001)
2.0 cm <sup>b</sup>	18 56 22.52	2 20 27.3	0.57×0.45	—	0.082(0.000)	0.242(0.001)
1.3 cm <sup>a</sup>	18 56 22.528(0.01)	2 20 27.619(0.02)	0.36×0.24;12.6	0.66×0.19;23.7	0.080(0.006)	0.255(0.015)
1.3 mm <sup>a</sup>	18 56 22.554(0.06)	2 20 27.705(0.05)	3.38×3.05;76.1	2.24×1.29;73.6	0.811(0.030)	1.056(0.017)
0.85 mm <sup>c</sup>	18 56 22.530(0.48)	2 20 24.447(0.54)	14.00×14.00; 0	18.64×14.99;-11.7	4.801(0.259)	11.712(0.201)
0.45 mm <sup>c</sup>	18 56 22.425(0.51)	2 20 25.306(0.56)	8.00×8.00; 0	11.72×10.04;-17.7	21.328(2.003)	60.701(1.550)

<sup>a</sup> SMA and VLA data from this work.

<sup>b</sup> VLA data from Kurtz et al. (1994).

<sup>c</sup> JCMT data from archive (<http://www.jach.hawaii.edu/JCMT/archive/>).

### 3.1. Spectra

Figure 1 shows the SMA 4 GHz continuum-free spectra extracted from the line-cubes at the position of the 1.3 mm continuum peak smoothed to 4.25 km s<sup>-1</sup> channel spacing. The original spectral resolution of 0.85 km s<sup>-1</sup> was used for the data analysis. For the spectral identification, we checked the line observations of G20.08-0.14N (Galván-Madrid et al. 2009). Then, the rest frequencies were mainly assigned with spectral catalogs of JPL (Pickett et al. 1998), CDMS (Müller et al. 2005), and SPLATALOGUE<sup>11</sup>. Finally, we identified 25 transitions from 8 molecular species and their isotopologues. The relevant line parameters are listed in Table 1.

Figures 2 and 3 show Gaussian fits of several lines including CO (2-1), <sup>13</sup>CO (2-1), <sup>13</sup>CS (5-4), OCS (19-18), SO<sub>2</sub> 11(1,11)-10(0,10), <sup>34</sup>SO<sub>2</sub> 22(2,20)-22(1,21), <sup>34</sup>SO<sub>2</sub> 13(2,12)-13(1,13), H30α, H38β, CH<sub>3</sub>CN (12-11), and CH<sub>3</sub>CCH (13-12). The systemic velocity  $V_{sys} \approx 52.5$  km s<sup>-1</sup> was derived from the mean value of the velocities from Gaussian fits. The spectra were extracted from the position of the 1.3 mm continuum peak. The channel spacings are 0.85 and 1.70 km s<sup>-1</sup> for Figures 2 and 3, respectively. Since the spectral profiles are absorbed strongly at the line center, we assumed that the spectral features are from self-absorption and missing flux, and then masked the absorption dip to make Gaussian fitting using CLASS software. The CH<sub>3</sub>CN 12(0)-11(0) with 12(1)-11(1) and CH<sub>3</sub>CCH 13(0)-12(0) with 13(1)-12(1) are blended, so they are not fitted. The fitted line parameters are listed in Table 1.

Figure 4 shows the VLA absorption spectra of NH<sub>3</sub> (2, 2) and (3, 3) at the position of the 1.3 cm continuum peak. The channel spacing is 0.617 km s<sup>-1</sup>. We only fitted the main lines of NH<sub>3</sub> with Gaussian profiles, because the satellite lines are too noisy to be identified. The fitted line parameters are listed in Table 1.

In Table 1, Column 1 lists the names of molecular species. Columns 2 – 3 list the transitions and rest frequencies of the molecules, respectively. Columns 4 – 7 list the Gaussian fitting results including integration flux, central line velocity, full width at half-maximum (FWHM), and peak intensity, respectively. Uncertainties are shown in parentheses following each Gaussian

fitting result.

### 3.2. Moment Maps

Figure 5 shows (A) velocity-integrated contours of CO (2-1) superimposed on the 1.3 mm continuum image, (B) velocity-integrated contours of <sup>13</sup>CO (2-1) superimposed on the 1.3 mm continuum image, (C) velocity-integrated contours of <sup>13</sup>CS (5-4) superimposed on the H30α emission image, and (D) velocity-integrated contours of SO<sub>2</sub> 11(1,11)-10(0,10) superimposed on the 3.6 cm continuum image. The blue and red contours show integrated emission from blue and red wings, and the velocity ranges are presented in the caption. The peak intensities of 1.3 mm continuum, H30α emission, and 3.6 cm continuum are 0.811 Jy beam<sup>-1</sup>, 61.37 Jy beam<sup>-1</sup> km s<sup>-1</sup>, and 0.163 Jy beam<sup>-1</sup>, respectively. The white cross indicates the position of the 1.3 cm continuum peak. The relevant coordinates and beam sizes are listed in Table 2. The white triangle indicates the positions of a water ( $\alpha$ (J2000) = 18<sup>h</sup>56<sup>m</sup>22<sup>s</sup>.550 and  $\delta$ (J2000) = 02°20'28"100) and OH maser ( $\alpha$ (J2000) = 18<sup>h</sup>56<sup>m</sup>22<sup>s</sup>.540 and  $\delta$ (J2000) = 02°20'28"100) (Forster & Caswell 1989; De Buizer et al. 2005), but no methanol masers have been detected (Caswell et al. 1995).

Figure 6 shows the velocity-integrated emission (moment 0, contours) superimposed on the intensity-weighted mean velocity (moment 1, color scale) maps. Figure 7 shows the velocity-integrated emission (moment 0, contours) superimposed on the velocity dispersion (moment 2, color scale) with respect to moment-1 velocity maps. The mapped molecular species include <sup>13</sup>CS (5-4), SO<sub>2</sub> 11(1,11)-10(0,10), CH<sub>3</sub>CCH 13(2)-12(2), and H30α.

Figure 8 shows the velocity-integrated contours of NH<sub>3</sub> (2, 2) and (3, 3) superimposed on the 1.3 cm continuum image. The velocity ranges are presented in the figure caption. The peak intensity of the 1.3 cm continuum is 80.29 mJy beam<sup>-1</sup>. The white cross indicates the position of 1.3 cm continuum peak. The relevant coordinates and beam sizes are listed in Table 2. The hollow and filled-black triangles indicate the positions of water maser ( $\alpha$ (J2000) = 18<sup>h</sup>56<sup>m</sup>22<sup>s</sup>.550 and  $\delta$ (J2000) = 02°20'28"100) and OH maser ( $\alpha$ (J2000) = 18<sup>h</sup>56<sup>m</sup>22<sup>s</sup>.540 and  $\delta$ (J2000) = 02°20'28"100) (Forster & Caswell 1989; De Buizer et al. 2005). The black “×” symbols indicate two separated H II regions: G35.578-0.030 to the west,

<sup>11</sup> <http://www.splatalogue.net/>

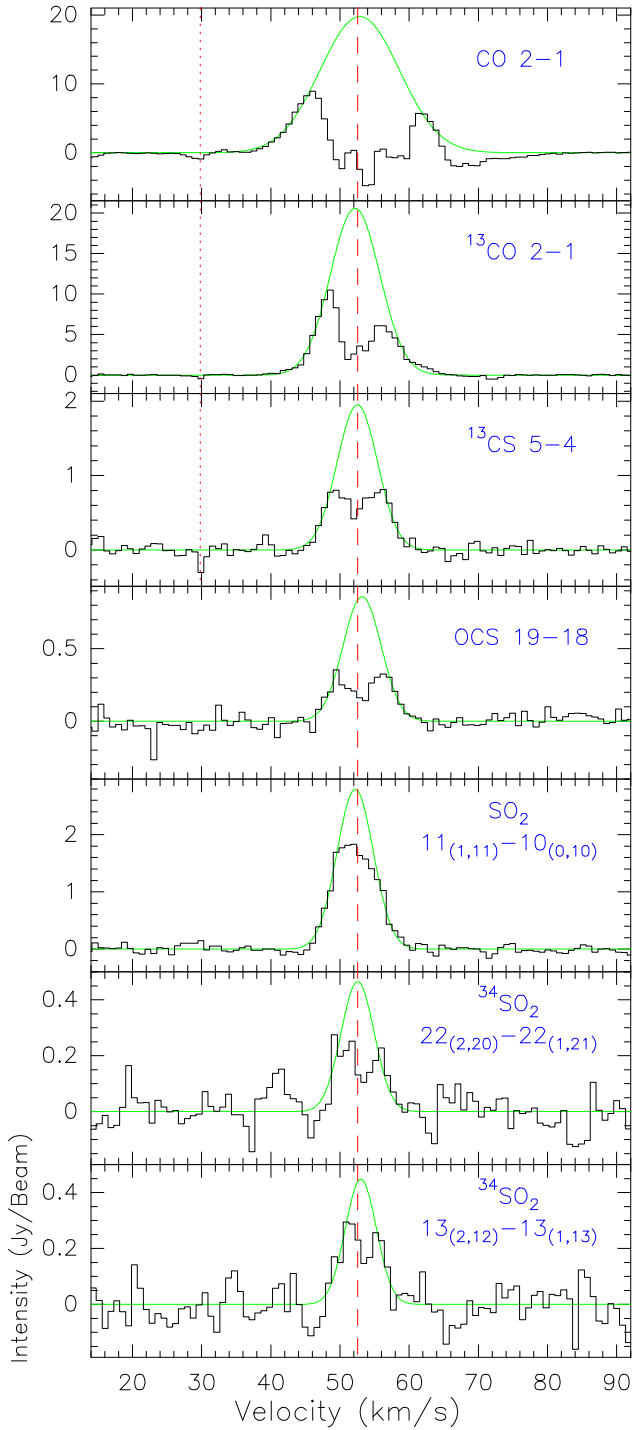


FIG. 2.— Molecular spectra at the position of the 1.3 mm continuum peak. The channel spacing in the plots is  $0.85 \text{ km s}^{-1}$ . The red dashed line crossing all the spectra denotes the systemic velocity ( $V_{sys} = 52.5 \text{ km s}^{-1}$ ), and the red dotted line indicates one absorption dip crossing spectra CO,  $^{13}\text{CO}$ , and  $^{13}\text{CS}$ . The green curves are Gaussian fitting lines.

and G35.578-0.031 to the east (Kurtz et al. 1994, 1999; De Buizer et al. 2005), however, our work shows that from the 1.3 cm continuum the eastern G35.578-0.031 is very faint. In fact, the G35.578-0.030 is the main research object in this work.

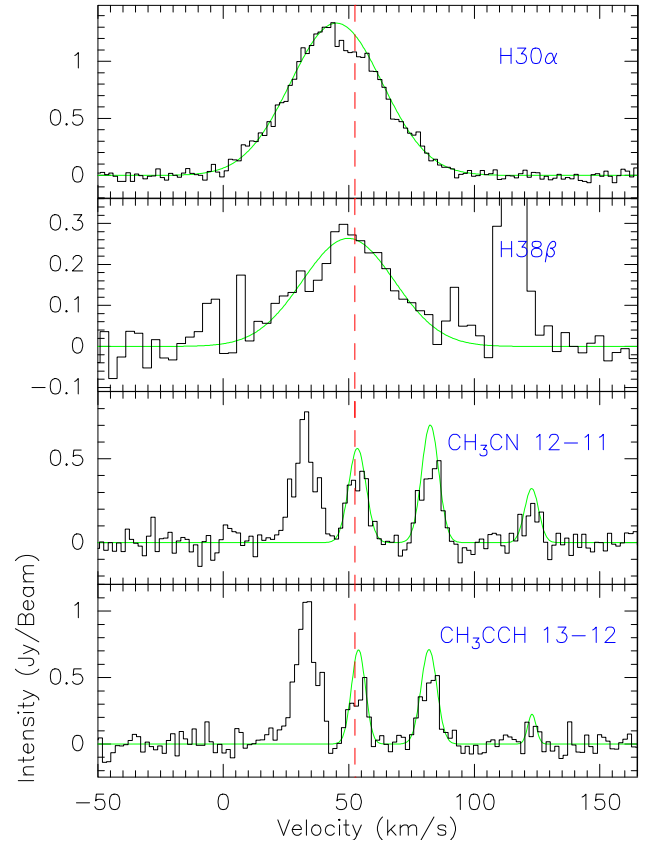


FIG. 3.— Molecular spectra at the position of the 1.3 mm continuum peak. The channel spacing is  $1.70 \text{ km s}^{-1}$  in the plots. The red dashed line denotes the systemic velocity ( $V_{sys} = 52.5 \text{ km s}^{-1}$ ), crossing the spectra H30 $\alpha$ , H38 $\beta$ , CH<sub>3</sub>CN 12(2)-11(2), and CH<sub>3</sub>CCH 13(2)-12(2). The green curves are Gaussian fitting lines.

Figure 9 shows the velocity-integrated contours of NH<sub>3</sub> (2, 2) and (3, 3) superimposed on the intensity-weighted mean velocity (moment 1, color scale) maps. Figure 10 shows the velocity-integrated contours of NH<sub>3</sub> (2, 2) and (3, 3) superimposed on the velocity dispersion (moment 2, color scale) with respect to moment-1 velocity maps.

### 3.3. PV Diagrams

Figure 11 shows the PV diagrams of 1.3 mm observations with P.A. =  $90^\circ$  at the position of the SMA 1.3 mm continuum peak. The mapped molecular species include CO (2-1),  $^{13}\text{CO}$  (2-1),  $^{13}\text{CS}$  (5-4), SO<sub>2</sub> 11(1,11)-10(0,10), H30 $\alpha$ , CH<sub>3</sub>CN 12(2)-11(2), CH<sub>3</sub>CN 12(3)-11(3), CH<sub>3</sub>CCH 13(2)-12(2), and CH<sub>3</sub>CCH 13(2)-12(2). The unit of contours is in Kelvin (DPFU<sub>1.3mm</sub>  $\sim 2.22 \text{ K per Jy beam}^{-1}$ ). The PV diagrams are useful to understand the infall, outflow, and/or rotation motions of molecular gas.

## 4. RESULTS AND DISCUSSIONS

### 4.1. Spectral Energy Distribution

Figure 12 exhibits the SED of the HC H II region G35.58-0.03 combining 3.6 cm, 2.0 cm, 1.3 cm, 1.3 mm, 0.85 mm, and 0.45 mm continuum data. Their fluxes are listed in Table 2. The modeling equations are described in Shi et al. (2010), one of which describes the

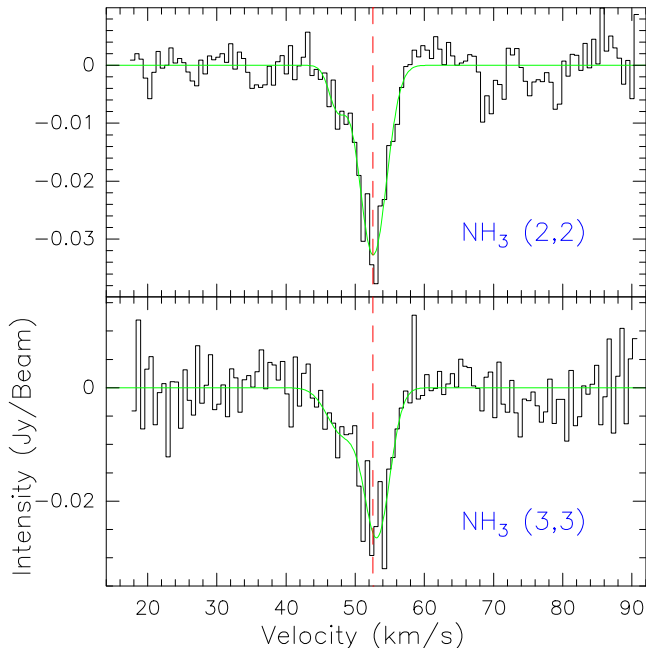


FIG. 4.— Molecular spectra of  $\text{NH}_3$  (2, 2) and (3, 3) at the position of the 1.3 cm continuum peak. The channel spacing is  $0.617 \text{ km s}^{-1}$  in the plots. The red dashed line, crossing the spectra, denotes the systemic velocity ( $V_{sys} = 52.5 \text{ km s}^{-1}$ ). The green curves are Gaussian fitting lines.

free-free emission of the ionized gas component, another the thermal emission from warm dust. The SED fitting results show that about 25% of the 1.3 mm continuum flux is contributed by the ionized gas component and about 75% by the warm dust component. Comparing the dense core seen in the high resolution 1.3 cm continuum with the low resolution 1.3 mm continuum data, we suggest that there exists a thick dust envelope surrounding the HC H II core. The dust emission arises from a much larger region than the free-free emission. Generally, the emission at the short wavelength side traces the dust in a disk/envelope system with a steep spectral index of  $\alpha_{\text{dust}} \gtrsim 2$ , while the emission at the long wavelength side is from ionized gas of thermal radio jet with a flat spectral index of  $\alpha_{\text{gas}} \lesssim 1$  (Reynolds 1986; Anglada et al. 1998; Choi et al. 2012). In this work, we obtain the two spectral indexes with  $\alpha_{\text{dust}} = 3.78 \pm 0.03$  and  $\alpha_{\text{gas}} = 0.32 \pm 0.04$ , which indicates a density gradient within the ionized gas (Franco et al. 2000). In addition, considering the 1.3 mm continuum flux contribution from the ionized gas component to be low, we derive an upper limit of 55% for the ionized gas component using the spectral index  $\alpha_{\text{gas}} = 0.32 \pm 0.04$ .

In Figure 12, the total continuum flux is higher than the fit for 0.85 mm and 0.45, because of their lower resolutions. However the 1.3 cm continuum data can resolve the G35.58-0.03 into two sources (see Figure 8), which leads to a low flux. So, for the 1.3 cm continuum, we used “IMSTAT” (AIPS task) to obtain a total flux of  $\sim 255 \text{ mJy}$  and a peak flux of  $\sim 80.29 \text{ mJy beam}^{-1}$  within a region of  $\sim 1''.5 \times 1''.5$ . If doing “JMFIT” (AIPS task) with one Gaussian component, we will just obtain a total flux with  $184.4 \pm 2.7 \text{ mJy}$  and the peak flux with  $68.8 \pm 0.7 \text{ mJy beam}^{-1}$  at 1.3 cm. Due to the data con-

tamination, the SED fitting is rough relatively.

#### 4.2. Hypercompact H II Region

The HC H II region G35.58-0.03 is unresolved in the SMA 1.3 mm continuum observation in Figure 5, while it presents an elongated distribution with  $\text{PA} = 23^\circ 7$  in the VLA 1.3 cm continuum observation in Figure 8. The elongated distribution has a direction consistent with an outflow (see Section 4.5.2), suggesting that there exists interaction between the ionized and molecular gas. We derive an intrinsic size  $\theta_s = \sqrt{0''.655 \times 0''.192} \approx 0''.354$  for the HC H II core from the deconvolved beam size of the 1.3 cm continuum observation. For optically thin ionized gas and local thermodynamic equilibrium (LTE) condition, one can derive the electron temperature  $T_e^*$  based on the 1.3 mm continuum flux density and the  $\text{H}30\alpha$  line intensity (Gordon & Sorochenko 2002; Wilson et al. 2009; Shi et al. 2010):

$$T_e^* = \left[ \left( \frac{6985}{\alpha(\nu, T_e)} \right) \left( \frac{\Delta V_{\text{H}30\alpha}}{\text{km s}^{-1}} \right)^{-1} \left( \frac{S_{1.3\text{mm}}^{\text{gas}}}{S_{\text{H}30\alpha}} \right) \times \left( \frac{\nu}{\text{GHz}} \right)^{1.1} \left( 1 + \frac{N(\text{He}^+)}{N(\text{H}^+)} \right)^{-1} \right]^{0.87}, \quad (1)$$

where  $\alpha(\nu, T_e) \sim 1$  is a slowly varying function tabulated by Mezger & Henderson (1967), and  $\frac{N(\text{He}^+)}{N(\text{H}^+)} \sim 0.096$  was adopted (Mehringer 1994).  $S_{1.3\text{mm}}^{\text{gas}} = 0.811 \times 55\% \text{ Jy beam}^{-1}$  (upper limit from Section 4.1) and  $S_{\text{H}30\alpha} = 1.34 \text{ Jy beam}^{-1}$  are the peak flux density. Finally we get an electron temperature  $T_e^* = 5500 \text{ K}$ . Due to the uncertainty in the estimate of the dust contribution to  $S_{1.3\text{mm}}$ , the error on the temperature might be high. This temperature is a lower limit due to the uncertain SED fitting flux density, and the 1.3 mm data in relatively low resolution tracing also extended envelope material.

The emission measure (EM) is an important parameter for the HC H II region. We derive the EM parameter from equation in Wilson et al. (2009) and Shi et al. (2010) with

$$\text{EM} = 7.1 \text{ pc cm}^{-6} \left( \frac{S_L}{\text{Jy}} \right) \left( \frac{\lambda}{\text{mm}} \right) \left( \frac{T_e}{\text{K}} \right)^{1.5} \times \left( \frac{\Delta V}{\text{km s}^{-1}} \right) \left( \frac{\theta_s}{\text{arcsec}} \right)^{-2}. \quad (2)$$

Assuming  $T_e \approx T_e^*$ , the electron temperature is estimated by  $T_e \sim 5500 \text{ K}$  for the HC H II core. The intrinsic size is  $\theta_s \approx 0''.354$  for the H II region. For the  $\text{H}30\alpha$  line, the peak line intensity is  $S_L = 1.43 \text{ Jy}$ , and the FWHM is  $\Delta V = 43.16 \text{ km s}^{-1}$ . The observing wavelength is  $\lambda = 1.3 \text{ mm}$ . Based on the parameters above, we obtain an  $\text{EM} = 1.9 \times 10^9 \text{ pc cm}^{-6}$  for the HC H II region. The corresponding volume electron density is estimated by  $n_e = 3.3 \times 10^5 \text{ cm}^{-3}$  from  $\text{EM} = n_e^2 L f_V$  ( $L$  and  $f_V$  is the path length and volume filling factor, respectively), assuming the HC H II core size is  $L = 10.2 \times \tan(0''.354) \text{ kpc} = 3714 \text{ AU}$ , and  $f_V = 1$ . The continuum optical depth  $\tau_c$  can be obtained from the

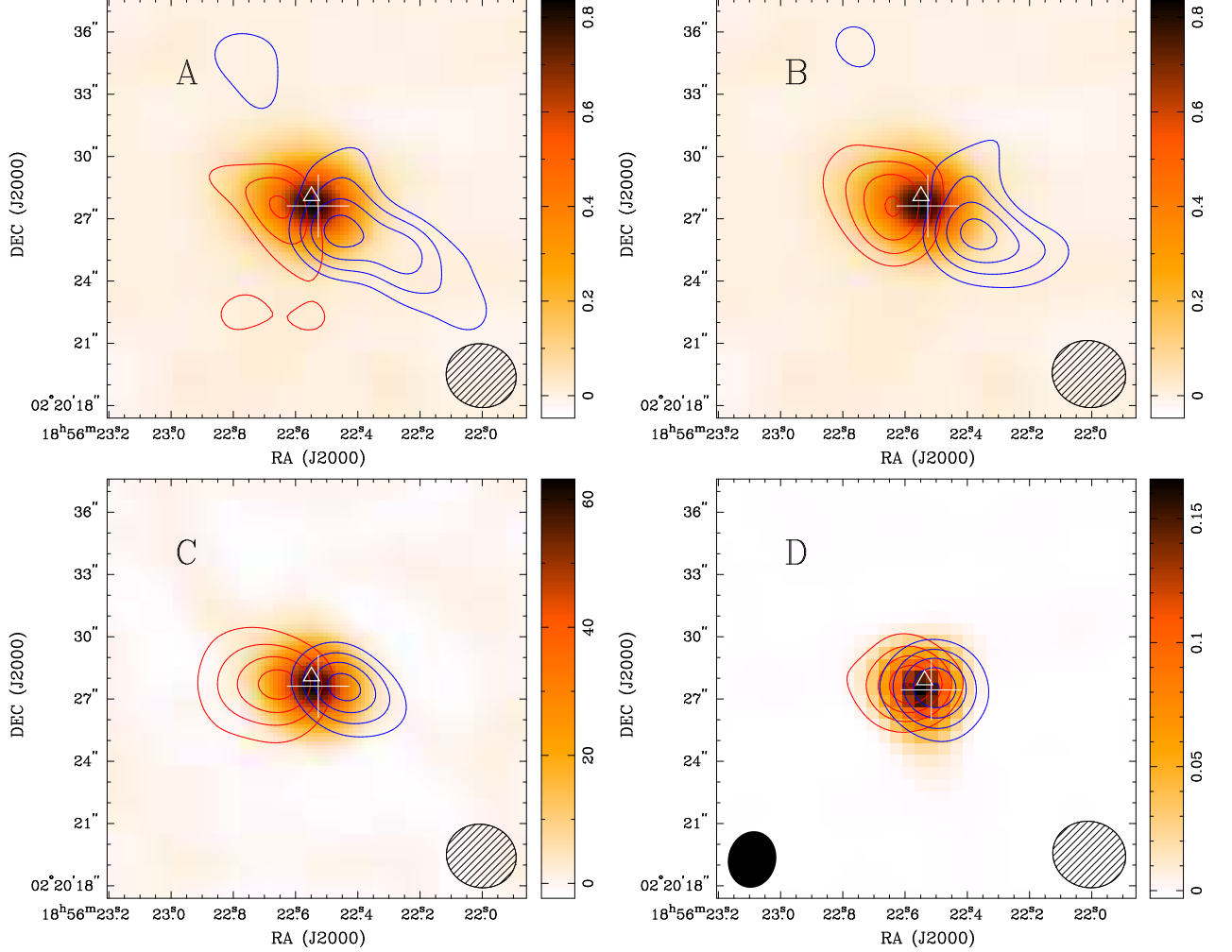


FIG. 5.— (A) Velocity-integrated contours of CO (2-1) superimposed on the 1.3 mm continuum image. The blue contours of  $[45, 50]$  km s $^{-1}$  are 3, 4, 5, 6  $\times 1.70$  Jy beam $^{-1}$  km s $^{-1}$ , and the red contours of  $[59, 65]$  km s $^{-1}$  are 3, 4, 5  $\times 0.79$  Jy beam $^{-1}$  km s $^{-1}$ , respectively. The 1.3 mm continuum peak is 0.811 Jy beam $^{-1}$ . (B) Velocity-integrated contours of  $^{13}\text{CO}$  (2-1) superimposed on the 1.3 mm continuum image. The blue contours of  $[40, 50]$  km s $^{-1}$  are 3, 4, 5, 6  $\times 0.18$  Jy beam $^{-1}$  km s $^{-1}$ , and the red contours of  $[56, 66]$  km s $^{-1}$  are 3, 4, 5, 6  $\times 1.28$  Jy beam $^{-1}$  km s $^{-1}$ , respectively. The 1.3 mm continuum peak is 0.811 Jy beam $^{-1}$ . (C) Velocity-integrated contours of  $^{13}\text{CS}$  (5-4) superimposed on the H30 $\alpha$  velocity-integrated image. The blue contours of  $[46, 51]$  km s $^{-1}$  are 3, 5, 7, 9  $\times 0.41$  Jy beam $^{-1}$  km s $^{-1}$ , and the red contours of  $[54, 60]$  km s $^{-1}$  are 3, 5, 7, 9  $\times 0.57$  Jy beam $^{-1}$  km s $^{-1}$ , respectively. The H30 $\alpha$  flux peak is 61.37 Jy beam $^{-1}$  km s $^{-1}$  for integration range  $[0, 90]$  km s $^{-1}$ . (D) Velocity-integrated contours of SO $_2$  11(1, 11) – 10(0, 10) superimposed on the 3.6 cm continuum image. The blue contours of  $[46, 51]$  km s $^{-1}$  are 3, 5, 7, 9, 11  $\times 0.62$  Jy beam $^{-1}$  km s $^{-1}$ , and the red contours of  $[54, 60]$  km s $^{-1}$  are 3, 5, 7, 9, 11  $\times 0.29$  Jy beam $^{-1}$  km s $^{-1}$ , respectively. The 3.6 cm continuum peak is 0.163 Jy beam $^{-1}$ . The white cross indicates the position of 1.3 cm continuum peak. The white triangle indicates the position of water and OH masers. The synthesized beam of 1.3 mm and 1.3 cm data are in hatched and solid ellipses, respectively.

equation in Mezger & Henderson (1967) with

$$\tau_c = 0.08235 \alpha(\nu, T_e) \left( \frac{\nu}{\text{GHz}} \right)^{-2.1} \left( \frac{T_e}{\text{K}} \right)^{-1.35} \times \left( \frac{\text{EM}}{\text{pc cm}^{-6}} \right). \quad (3)$$

$\tau_c \approx 0.015$  is finally derived, assumed  $\alpha(\nu, T_e) \sim 1$ . However, the same formula (3) gives an optical depth of about 1.8, if the frequency of the 1.3 cm continuum is used. The derived parameters above indicate that the H30 $\alpha$  line is optically thin, and traces a very dense region ( $< 3714$  AU) with high temperature. In addition, it is necessary to further use RRLs as tracers to study the regions with

high density and temperature.

We employ the Lyman continuum photon number ( $N_L$ ) and the excitation parameter ( $U$ ) to infer the corresponding star type. The corresponding equations are expressed (Rubin 1968; Panagia 1973; Mezger et al. 1974; Matsakis et al. 1976):

$$N_L = 4.761 \times 10^{48} \text{s}^{-1} \alpha(\nu, T_e)^{-1} \left( \frac{\nu}{\text{GHz}} \right)^{0.1} \left( \frac{D}{\text{kpc}} \right)^2 \times \left( \frac{S_\nu^{\text{gas}}}{\text{Jy}} \right) \left( \frac{T_e}{\text{K}} \right)^{-0.45}, \quad (4)$$

$$U = 2.706 \times 10^{-16} \text{pc cm}^{-2} \left( \frac{T_e}{\text{K}} \right)^{4/15} \left( \frac{N_L}{\text{s}^{-1}} \right)^{1/3}, \quad (5)$$



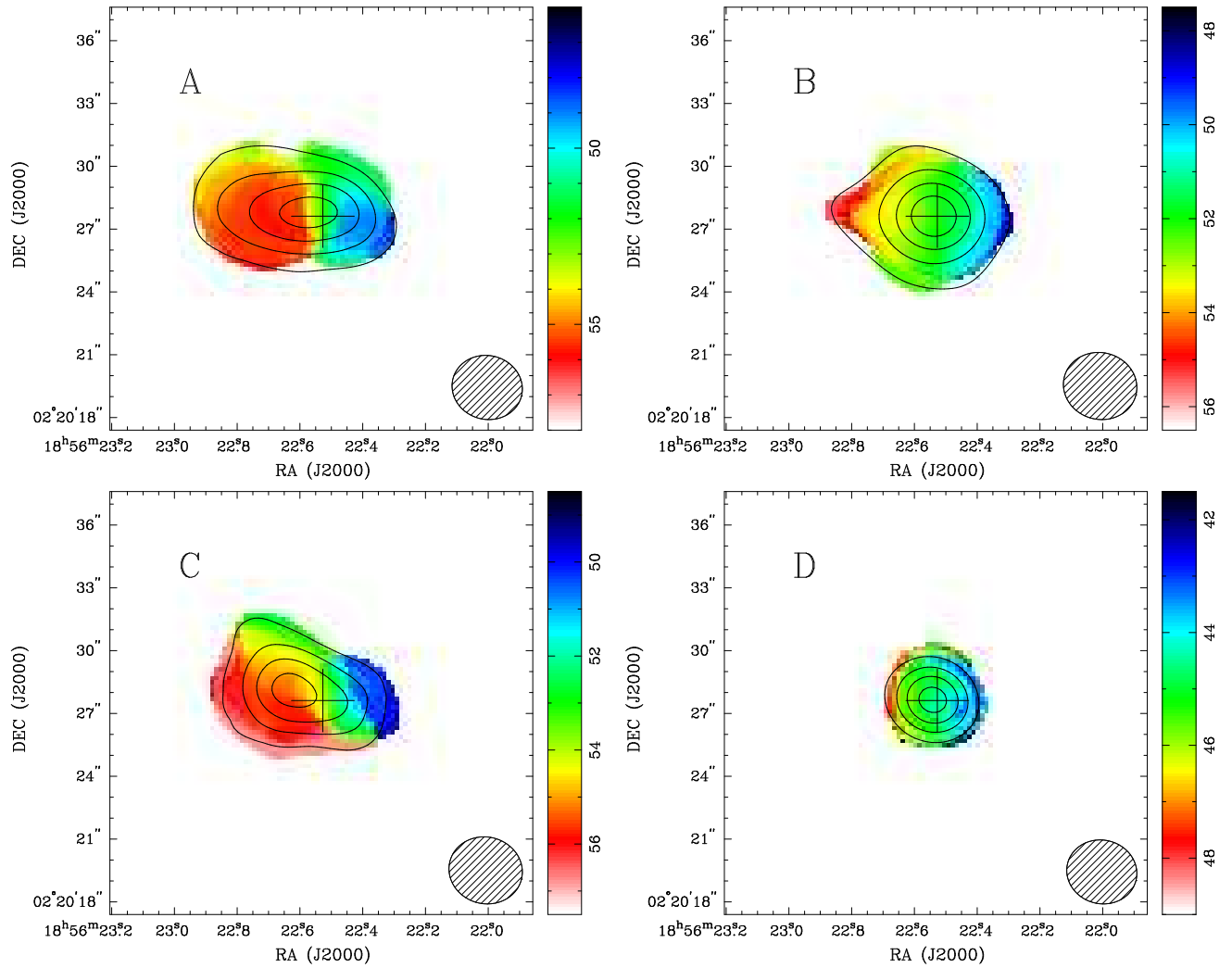


FIG. 6.— Velocity-integrated emission (moment 0, *contours*) superimposed on the intensity-weighted mean velocity (moment 1, *color scale*) maps. (A) Contours of  $^{13}\text{CS}$  (5-4) are 3, 5, 7,  $9 \times 0.87 \text{ Jy beam}^{-1} \text{ km s}^{-1}$ ; (B) Contours of  $\text{SO}_2$  11(1,11)-10(0,10) are 3, 11, 19,  $27 \times 0.46 \text{ Jy beam}^{-1} \text{ km s}^{-1}$ ; (C) Contours of  $\text{CH}_3\text{CCH}$  13(2)-12(2) are 3, 5, 7,  $9 \times 0.41 \text{ Jy beam}^{-1} \text{ km s}^{-1}$ ; (D) Contours of  $\text{H}30\alpha$  are 3, 5, 7,  $9 \times 6.32 \text{ Jy beam}^{-1} \text{ km s}^{-1}$ . The black cross indicates the position of 1.3 cm continuum peak. The units of color bar are in  $\text{km s}^{-1}$ .

where  $D = 10.2 \text{ kpc}$  is the source distance from the Sun, and  $\alpha(\nu, T_e) \sim 1$  is used again. The upper limit of the continuum free-free emission flux is  $S_{\nu}^{\text{gas}} = 1.056 \times 55\% \text{ Jy}$  at 1.3 mm. Based on our previous derived parameters assuming optically thin and LTE conditions, we obtained two upper limits of  $N_L = 1.0 \times 10^{49} \text{ s}^{-1}$  and  $U = 58.0 \text{ pc cm}^{-2}$ . The inferred Lyman continuum photon number requires a massive star equivalent to a zero-age main-sequence star of type O6.5 located inside the HC H II region G35.58-0.03 (Panagia 1973).

#### 4.3. Radio Recombination Lines $\text{H}30\alpha$ and $\text{H}38\beta$

The observed line width,  $\Delta V$ , of the  $\text{H}30\alpha$  and  $\text{H}38\beta$  lines is produced by a combination of pressure broadening,  $\Delta V_P$ , and Doppler broadening,  $\Delta V_D$ . The Doppler broadening,  $\Delta V_D$ , includes thermal broadening,  $V_{\text{ther}}$ , which is due to the thermal motion of the particles, and the dynamical and/or turbulent broadening,  $\Delta V_{\text{dyn}}$ , which is due to infall, outflow, and/or rotation movements. In this work, the  $\text{H}38\beta$  line ( $S_{\text{H}38\beta} \approx 0.26$

$\text{Jy beam}^{-1}$ ) is much weaker than the  $\text{H}30\alpha$  line ( $S_{\text{H}30\alpha} \approx 1.34 \text{ Jy beam}^{-1}$ ), but both have almost the same line width ( $\Delta V_{\text{H}30\alpha} \approx 43.2 \text{ km s}^{-1}$ , and  $\Delta V_{\text{H}38\beta} \approx 43.2 \text{ km s}^{-1}$ ).

The broadening mechanisms can be described by the following equations (Gordon & Sorochenko 2002; Shi et al. 2010):

$$\Delta V = \sqrt{\Delta V_P^2 + \Delta V_D^2}, \quad (6)$$

$$\begin{aligned} \Delta V_D &= \sqrt{\Delta V_{\text{dyn}}^2 + \Delta V_{\text{ther}}^2} \\ &= \sqrt{\left(\frac{\Delta V_{\text{dyn}}}{\text{km s}^{-1}}\right)^2 + 0.0458 \left(\frac{T_e}{\text{K}}\right)} \text{ km s}^{-1}, \quad (7) \end{aligned}$$

$$\begin{aligned} \Delta V_P &= 3.74 \times 10^{-14} n^{4.4} \text{ km s}^{-1} \left(\frac{n_e}{\text{cm}^{-3}}\right) \times \\ &\quad \left(\frac{\lambda}{\text{mm}}\right) \left(\frac{T_e}{\text{K}}\right)^{-0.1}, \quad (8) \end{aligned}$$



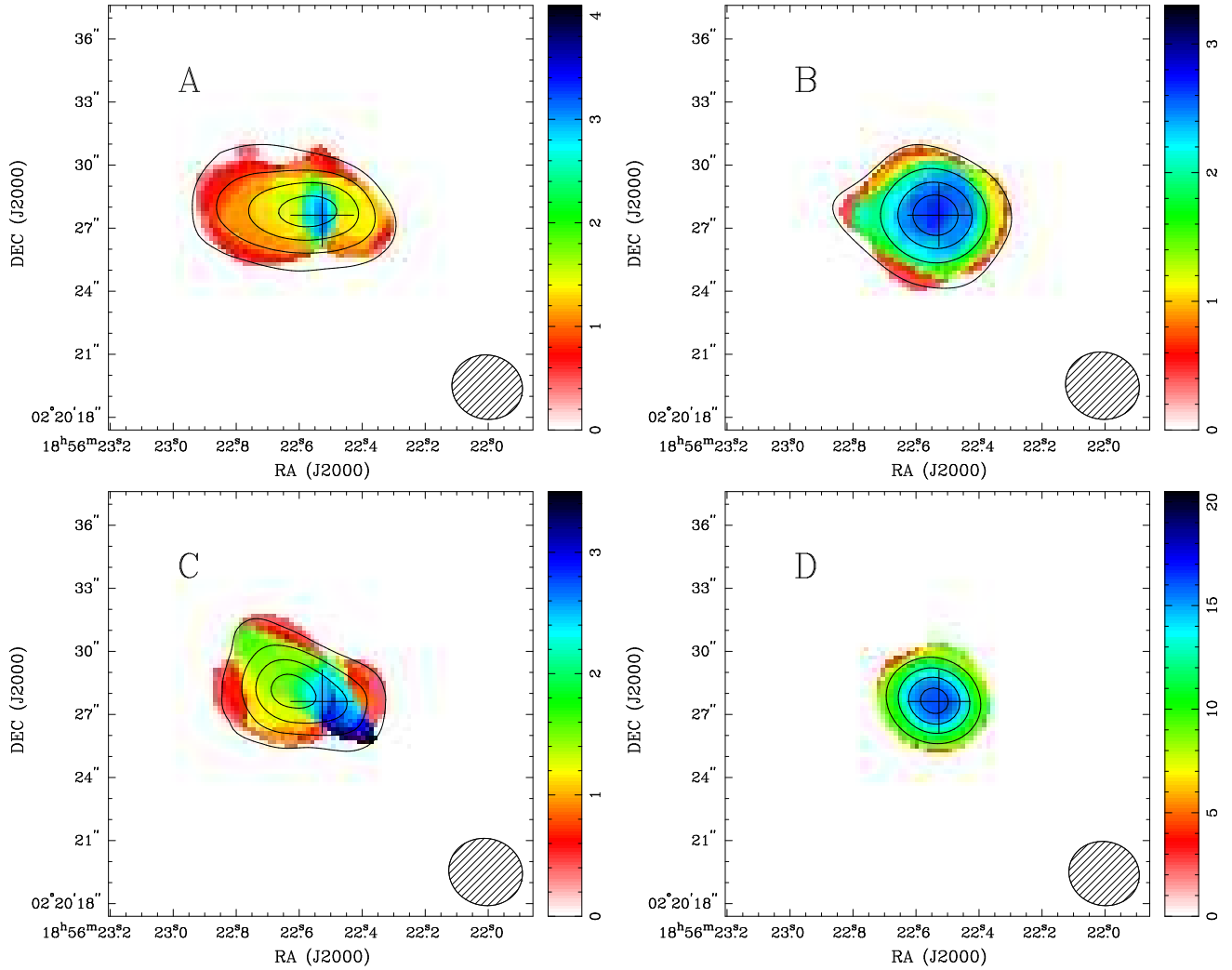


FIG. 7.— Velocity-integrated emission (moment 0, *contours*) superimposed on the velocity dispersion (moment 2, *color scale*) with respect to moment-1 velocity maps. (A) Contours of  $^{13}\text{CS}$  (5-4) are 3, 5, 7, 9  $\times 0.87 \text{ Jy beam}^{-1} \text{ km s}^{-1}$ ; (B) Contours of  $\text{SO}_2$  11(1,11)-10(0,10) are 3, 11, 19, 27  $\times 0.46 \text{ Jy beam}^{-1} \text{ km s}^{-1}$ ; (C) Contours of  $\text{CH}_3\text{CCH}$  13(2)-12(2) are 3, 5, 7, 9  $\times 0.41 \text{ Jy beam}^{-1} \text{ km s}^{-1}$ ; (D) Contours of  $\text{H}30\alpha$  are 3, 5, 7, 9  $\times 6.32 \text{ Jy beam}^{-1} \text{ km s}^{-1}$ . The black cross indicates the position of 1.3 cm continuum peak. The units of color bar are in  $\text{km s}^{-1}$ .

where  $n = 30$  and  $38$ , respectively, is the principal quantum number of the  $\text{H}30\alpha$  and  $\text{H}38\beta$  transitions. The broadening of the lines is derived using a local electron density ( $n_e \approx 3.3 \times 10^5 \text{ cm}^{-3}$ ) and electron temperature ( $T_e \approx 5500 \text{ K}$ ) for the HC H II region. The thermal broadening is  $\Delta V_{ther} \sim 15.87 \text{ km s}^{-1}$  for  $T_e = 5500 \text{ K}$ . Due to the relatively small principal quantum number, the pressure broadening ( $\Delta V_P(\text{H}30\alpha) = 0.02 \text{ km s}^{-1}$ , and  $\Delta V_P(\text{H}38\beta) = 0.06 \text{ km s}^{-1}$ ) contributes little to the total line width. The broadening contribution from the dynamical and/or turbulent broadening motions is  $\Delta V_{dyn}(\text{H}30\alpha) \approx 40.14 \text{ km s}^{-1}$  and  $\Delta V_{dyn}(\text{H}38\beta) \approx 40.16 \text{ km s}^{-1}$  for the  $\text{H}30\alpha$  and  $\text{H}38\beta$  lines, respectively. In addition, it also can be seen from the moment-1 map (Figure 6) and the PV diagram (Figure 11) that the  $\text{H}30\alpha$  line shows evidence of blueshifted and redshifted wings, which probably suggests infall, outflow, and/or rotation. Therefore, the  $\text{H}30\alpha$  line traces the high-temperature ionized gas, which is participating in

dynamical movements.

#### 4.4. Rotational Temperature

The rotational temperature diagram (RTD) method can be used to estimate the rotational temperature, if multiple transitions with different upper level energies are observed simultaneously (Goldsmith & Langer 1999; Araya et al. 2005). It may give an average excitation temperature of the specific molecule even in non-LTE cases (Qin et al. 2010). The corresponding parameters for the rotational temperature fitting are listed in Table 3. Due to the blending of  $\text{CH}_3\text{CN}$  12(0)-11(0) and 12(1)-11(1), and  $\text{CH}_3\text{CCH}$  13(0)-12(0) and 13(1)-12(1), we used their  $5\sigma$  as error in the fit. Following the RTD method from Qin et al. (2010), we get rotational temperatures of  $\sim 143 \pm 20 \text{ K}$  for  $\text{CH}_3\text{CN}$  (12-11), and  $\sim 95 \pm 17 \text{ K}$  for  $\text{CH}_3\text{CCH}$  (13-12) in Figure 13. The high rotational temperature suggests that the  $\text{CH}_3\text{CN}$  and  $\text{CH}_3\text{CCH}$  transitions originate from warm gas environment. The derived the rotational temperature (143 and

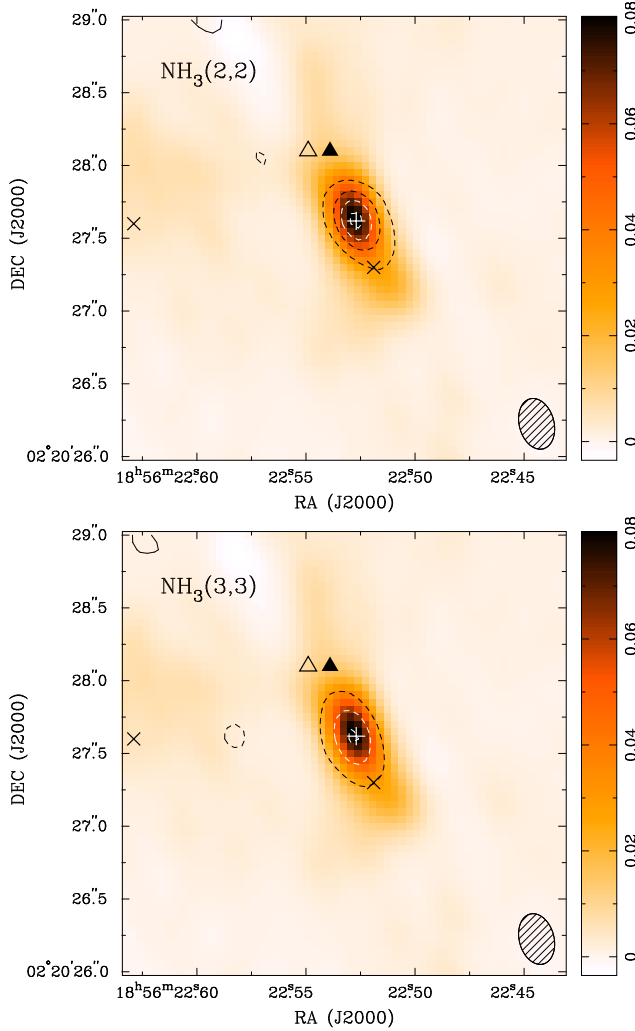


FIG. 8.— Velocity-integrated contours of  $\text{NH}_3$  (2, 2) and (3, 3) superimposed on the 1.3 cm continuum image. Contours of  $\text{NH}_3$  (2, 2) are -21, -15, -9, -3,  $3 \times 7.64 \text{ mJy beam}^{-1} \text{ km s}^{-1}$ ; Contours of  $\text{NH}_3$  (3, 3) are -15, -9, -3,  $3 \times 10.99 \text{ mJy beam}^{-1} \text{ km s}^{-1}$ . The 1.3 cm continuum peak is  $80.29 \text{ mJy beam}^{-1}$ . The white cross indicates the position of 1.3 cm continuum peak. The hollow and fill-black triangles indicate the positions of water and OH masers. The black symbols “x” indicate two UC H II regions from Kurtz et al. (1994, 1999).

95 K) of the two molecules from the HC H II region is equivalent to the canonical value (100 K) from the hot core stage.

#### 4.5. Infall, Outflow, and/or Rotation

##### 4.5.1. Infall

In Figure 2, the CO (2-1),  $^{13}\text{CO}$  (2-1),  $^{13}\text{CS}$  (5-4), OCS (19-18),  $^{34}\text{SO}_2$  22(2,20)-22(1,21), and  $^{34}\text{SO}_2$  13(2,12)-13(1,13) lines show double-peak profiles with blueshifted peaks stronger than redshifted peaks. To some extent, flux is missing in the line center of the CO (2-1) and  $^{13}\text{CO}$  (2-1) lines. However, the infall evidence can be determined using the red and blue shifted peaks alone. The red peaks of both  $\text{SO}_2$  11(1,11)-10(0,10) (in Figure 2) and  $\text{H}30\alpha$  (in Figure 3) are also absorbed, compared to the blue ones. Also the CO (2-1) spectrum shows a promi-

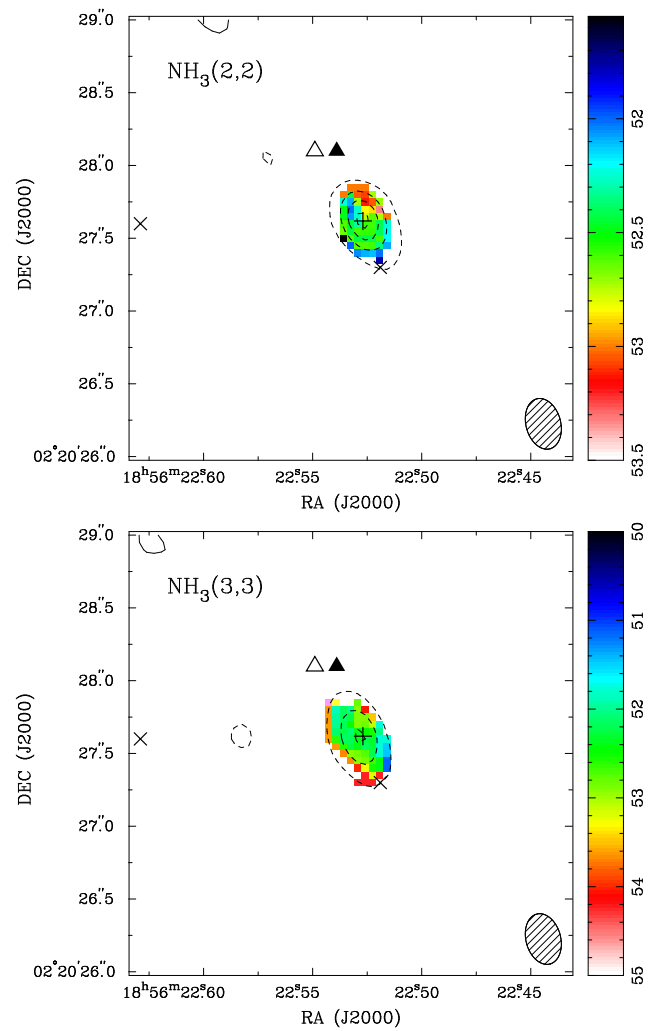


FIG. 9.— Velocity-integrated contours of  $\text{NH}_3$  (2, 2) and (3, 3) superimposed on the intensity-weighted mean velocity (moment 1, color scale) maps. Contours and symbols are the same as in Figure 8.

nent blue shifted profile. In Figure 11, the PV diagrams of 1.3 mm lines except for  $\text{H}30\alpha$  show obvious velocity gradients. These spectral features indicate an infalling circumstellar envelope surrounding the compact core of the HC H II region G35.58-0.03.

The rapidly infalling envelope can provide the force to prevent the expansion of the H II region. The infall velocity is  $V_{\text{in}} = \sim 1.5 \text{ km s}^{-1}$  by comparing the systemic velocity  $\sim 52.5 \text{ km s}^{-1}$  with the velocity of the redshifted absorbing dip ( $\sim 54 \text{ km s}^{-1}$ ) in CO (2-1), OCS (19-18),  $^{34}\text{SO}_2$  22(2,20)-22(1,21), and  $^{34}\text{SO}_2$  13(2,12)-13(1,13). Because of the CO lines being optically thick, and the missing flux due to a lack of short spacing data, we use the 1.3 mm continuum to derive the column density and mass of the H II region envelope. The mean dust temperature can be estimated as a lower limit of  $\sim 95 \pm 17 \text{ K}$  from the rotational temperature of  $\text{CH}_3\text{CN}$  and  $\text{CH}_3\text{CCH}$  in Section 4.4. Assuming an average grain radius of  $0.1 \mu\text{m}$  and grain density of  $3 \text{ g cm}^{-3}$  and a gas to dust ratio of 100, the hydrogen column density is given

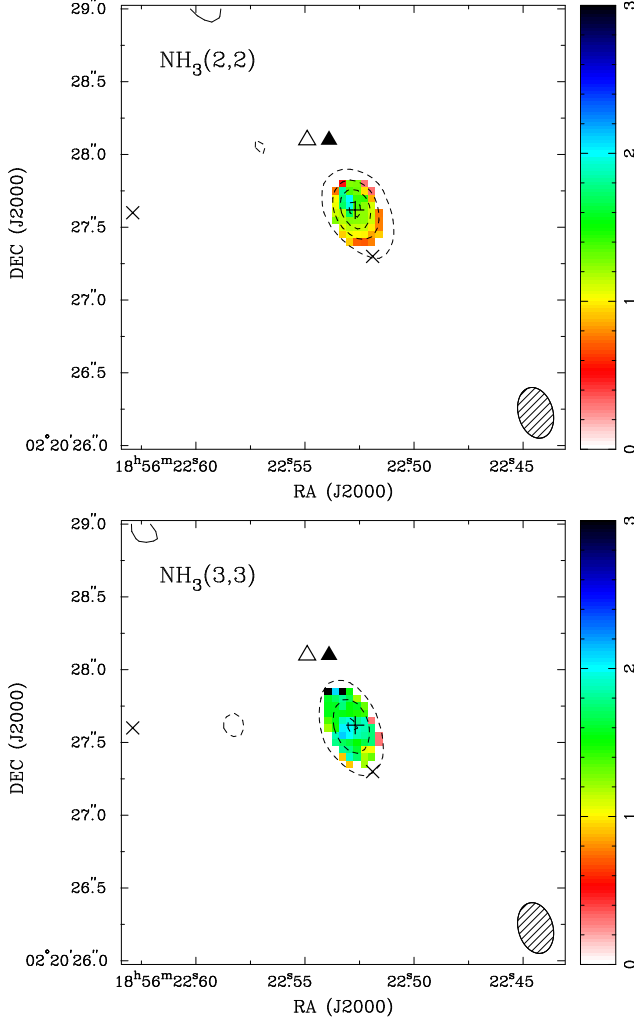


FIG. 10.— Velocity-integrated contours of  $\text{NH}_3$  (2, 2) and (3, 3) superimposed on the velocity dispersion (moment 2, *color scale*) with respect to moment-1 velocity maps. Contours and symbols are the same as in Figure 8.

by the formula (Lis et al. 1991)

$$N_{\text{H}_2} = 8.1 \times 10^{17} \text{cm}^{-2} \frac{e^{h\nu/kT} - 1}{Q(\nu)\Omega} \left( \frac{S_\nu^{\text{dust}}}{\text{Jy}} \right) \left( \frac{\nu}{\text{GHz}} \right)^{-3} \quad (9)$$

where  $T \sim 95$  K is the mean dust temperature,  $Q(\nu) \sim 2 \times 10^{-5}$  is grain emissivity at frequency 231 GHz,  $S_\nu^{\text{dust}} = 1.056 \times 75\%$  Jy is the warm dust emission of the continuum at 1.3 mm peak, and  $\Omega$  is the beam solid angle. The derived hydrogen column density is  $N_{\text{H}_2} = 1.7 \times 10^{24} \text{cm}^{-2}$ , so that the volume density is  $n_{\text{H}_2} = 3.5 \times 10^6 \text{cm}^{-3}$ . In addition, the total envelope mass in a beam size can be estimated from the 1.3 mm continuum using the formula (Lis et al. 1991)

$$M_{\text{H}_2} = 1.3 \times 10^4 M_\odot \frac{e^{h\nu/kT} - 1}{Q(\nu)} \left( \frac{S_\nu^{\text{dust}}}{\text{Jy}} \right) \times \left( \frac{\nu}{\text{GHz}} \right)^{-3} \left( \frac{D}{\text{kpc}} \right)^2. \quad (10)$$

Assuming the molecular mass ratio  $M_{\text{env}}/M_{\text{H}_2} = 1.36$ , we obtain a total envelope mass  $M_{\text{env}} = 538 M_\odot$  as an upper limit. The infall rate of the envelope material can be estimated by

$$\dot{M}_{\text{in}} = 2.1 \times 10^{-11} M_\odot \text{yr}^{-1} \left( \frac{V_{\text{in}}}{\text{km s}^{-1}} \right) \left( \frac{n_{\text{H}_2}}{\text{cm}^{-3}} \right) \times \left( \frac{D}{\text{kpc}} \right)^2 \left( \frac{\theta_{\text{in}}}{\text{arcsec}} \right)^2, \quad (11)$$

where  $\theta_{\text{in}} = \sqrt{2''238 \times 1''285} \approx 1''696$  (from the deconvolved beam size of the 1.3 mm continuum observation) is the diameter of the infalling region,  $D$  is the distance to the source, and  $V_{\text{in}} \sim 1.5 \text{km s}^{-1}$  is the infall velocity. A lower limit of the infall rate of  $0.033 M_\odot \text{yr}^{-1}$  is inferred with the derived parameters. The momentum of the infalling gas per year is  $\sim 0.050 M_\odot \text{km s}^{-1}$ .

A high accretion rate is necessary to form an O star, however, Walmsley (1995) reports a high “critical accretion rate” to “choke off” an H II region formation. In this work, we obtain an infall rate of  $0.033 M_\odot \text{yr}^{-1}$ , which is high enough to quench any H II region and to overcome the radiation pressure from central star. The observed lines at 1.3 cm do not show any infalling features (see Section 4.6). This suggests that the accretion in the inner part might already be halted.

#### 4.5.2. Outflow

Figure 2 shows the CO (2-1) spectrum with very broad wings between  $\sim 38$  and  $\sim 65 \text{km s}^{-1}$ . High-velocity gas can be easily identified in the PV diagrams of Figure 11 and is exhibited in Figure 5. The Gaussian fitting FWHM of CO (2-1) spectrum is  $\sim 13.53 \text{km s}^{-1}$ . In all spectra shown in Figures 2, 3, and 4, the narrowest two spectra are  $\text{CH}_3\text{CCH}$  13(4)-12(4) with FWHM  $\approx 3.99 \text{km s}^{-1}$ , and  $\text{NH}_3$  (3, 3) with FWHM  $\approx 4.35 \text{km s}^{-1}$ . Figure 5 exhibits a bipolar outflow in the tracers CO (2-1),  $^{13}\text{CO}$  (2-1),  $^{13}\text{CS}$  (5-4), and  $\text{SO}_2$  11(1,11)-10(0,10). The two lobes can also be identified from the intensity-weighted mean velocity in Figure 6. Especially, there is one consistent direction of the velocity gradient between H30 $\alpha$  and other molecular gas seen from Figure 6D with 6A, 6B, and 6C, indicating that the ionized outflow is acting along with the molecular bipolar outflow. This is evidence for an ionized outflow driving a molecular outflow (Klaassen et al. 2013). The H30 $\alpha$  line has a large velocity dispersion at the position of 1.3 cm continuum peak in Figure 7, suggesting its driving source position. 1.3 mm, 1.3 cm, and 3.6 cm continuum locations are well correlated with the outflow. Water and OH masers were also found near the position of the continuum peaks. This shows that the outflow is very active. There are small differences in the outflow directions seen in Figure 5. We argue that  $^{13}\text{CS}$  (5-4) and  $\text{SO}_2$  11(1,11)-10(0,10) outflows are possibly contaminated with infall and rotation. Furthermore, the CO (2-1) and  $^{13}\text{CO}$  (2-1) outflows, showing also lobes to the north (see Figure 5) in the direction perpendicular to the bipolar outflow, maybe also be blended with infall and rotation.

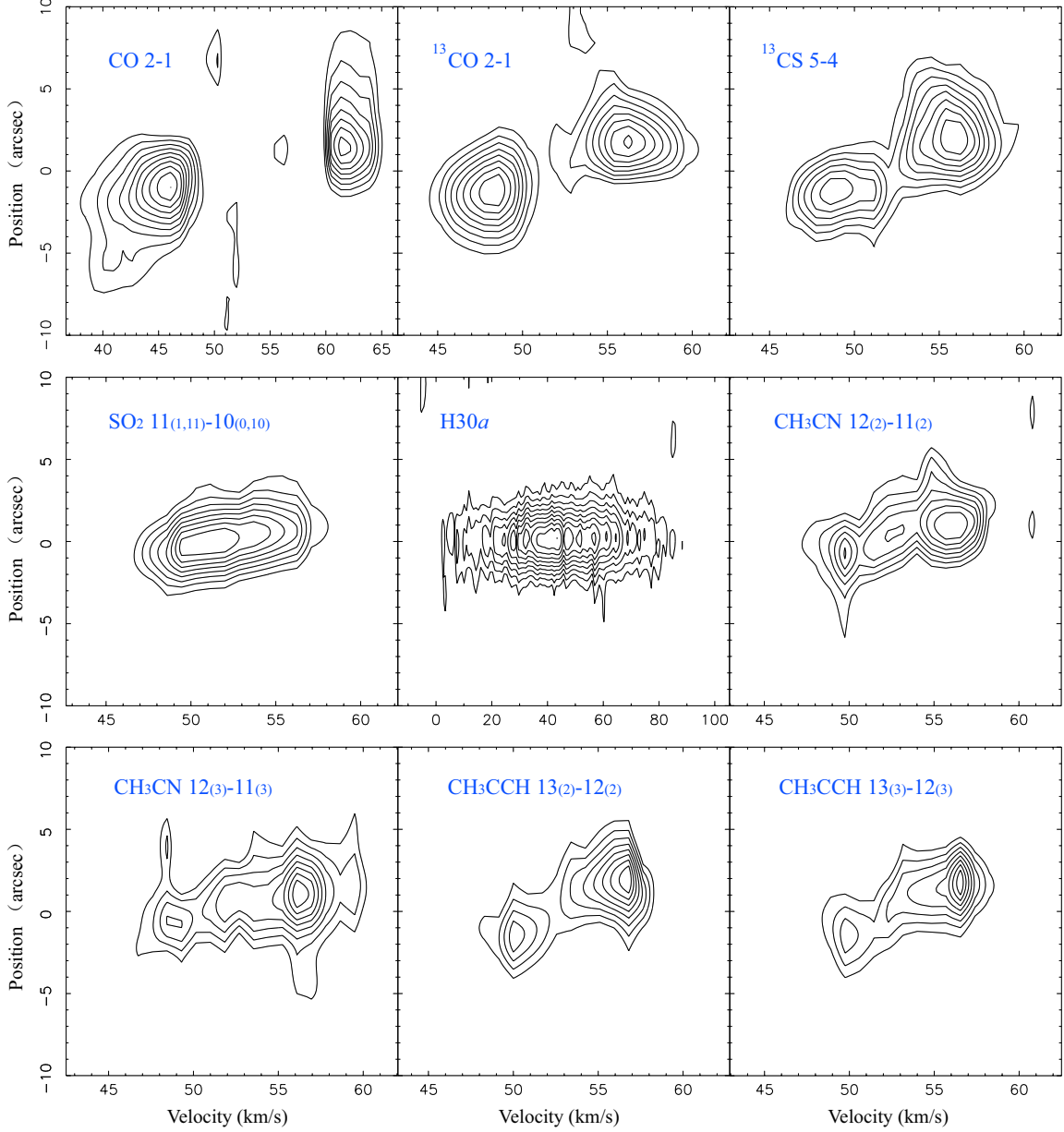


FIG. 11.— PV diagrams of 1.3 mm observations with P.A. =  $90^\circ$  at the position of the 1.3 mm continuum peak. Contours of CO (2-1) are 2.30, 4.60, 6.89, 9.19, 11.5, 13.8, 16.1, 18.4, 20.7 K; Contours of  $^{13}\text{CO}$  (2-1) are 5.47, 8.20, 10.9, 13.7, 16.4, 19.1, 21.9, 24.6 K; Contours of  $^{13}\text{CS}$  (5-4) are 0.616, 0.924, 1.23, 1.54, 1.85, 2.16, 2.47, 2.77 K; Contours of  $\text{SO}_2$  11(1,11)-10(0,10) are 0.839, 1.26, 1.68, 2.10, 2.52, 2.94, 3.36, 3.78 K; Contours of  $\text{H}30\alpha$  are 0.317, 0.634, 0.951, 1.27, 1.58, 1.90, 2.22, 2.54, 2.85 K; Contours of  $\text{CH}_3\text{CN}$  12(2)-11(2) are 0.361, 0.481, 0.601, 0.721, 0.841, 0.962, 1.08 K; Contours of  $\text{CH}_3\text{CN}$  12(3)-11(3) are 0.304, 0.456, 0.608, 0.760, 0.912, 1.06, 1.22, 1.37 K; Contours of  $\text{CH}_3\text{CCH}$  13(2)-12(3) are 0.423, 0.635, 0.847, 1.06, 1.27, 1.48, 1.69, 1.90 K; Contours of  $\text{CH}_3\text{CCH}$  13(3)-12(3) are 0.501, 0.751, 1.00, 1.25, 1.50, 1.75, 2.00, 2.25 K.

Many studies show that low-velocity molecular gas toward the core is usually optically thick (Goldsmith et al. 1984; Snell et al. 1984). Under conditions of local thermodynamic equilibrium (LTE), we assume that both the blueshifted and redshifted lobes are optically thin for  $^{13}\text{CO}$  (2-1). The relation between opacities and the ratio of  $^{12}\text{CO}$  (2-1) to  $^{13}\text{CO}$  (2-1) main-beam brightness temperature (Myers et al. 1983) is

$$\frac{T_{\text{MB}}(^{12}\text{CO})}{T_{\text{MB}}(^{13}\text{CO})} = \frac{1 - e^{-\tau^{12}}}{1 - e^{-\tau^{13}}}, \quad (12)$$

where we assume  $\tau^{12} = 89\tau^{13}$  (Lang 1980; Garden et al. 1991). Furthermore, the excitation temperature  $T_{\text{ex}}$  is derived from the equation of radiative transfer

$$\begin{cases} T_{\text{MB}} = f[J(T_{\text{ex}}) - J(T_{\text{bg}})][1 - e^{-\tau}] \\ J(T) = T_0/[e^{T_0/T} - 1] \end{cases}, \quad (13)$$

where  $f$  is the beam filling factor,  $T_{\text{bg}} = 2.7$  K is background temperature, and  $T_0 = h\nu/k$  for the transition of  $^{13}\text{CO}$  (2-1) (Wong et al. 2008). We then obtain the molecular  $^{13}\text{CO}$  (2-1) column density  $N(^{13}\text{CO})$  from the

TABLE 3  
 ROTATIONAL TEMPERATURE DIAGRAM PARAMETERS<sup>a b</sup>

Molecule	Transition	$S\mu^2$ debye <sup>2</sup>	$E_u$ K	Flux Jy/beam-km/s	Intensity Jy/beam
(1)	(2)	(3)	(4)	(5)	(6)
CH <sub>3</sub> CN	12(0)-11(0)	183.74	69	6.39(0.39)	0.67(0.09)
CH <sub>3</sub> CN	12(1)-11(1)	182.46	76	4.02(0.59)	0.36(0.09)
CH <sub>3</sub> CN	12(2)-11(2)	178.64	97	4.12(0.35)	0.41(0.06)
CH <sub>3</sub> CN	12(3)-11(3)	172.26	133	4.44(0.44)	0.45(0.06)
CH <sub>3</sub> CN	12(4)-11(4)	163.32	183	1.30(0.50)	0.18(0.06)
CH <sub>3</sub> CN	12(5)-11(5)	151.84	247	0.93(0.36)	0.17(0.09)
CH <sub>3</sub> CN	12(6)-11(6)	137.80	325	1.07(0.33)	0.16(0.09)
CH <sub>3</sub> CCH	13(0)-12(0)	7.92	75	5.96(0.35)	0.63(0.09)
CH <sub>3</sub> CCH	13(1)-12(1)	7.87	82	3.34(0.35)	0.46(0.09)
CH <sub>3</sub> CCH	13(2)-12(2)	7.73	103	3.56(0.37)	0.40(0.08)
CH <sub>3</sub> CCH	13(3)-12(3)	7.50	139	4.65(0.38)	0.50(0.07)
CH <sub>3</sub> CCH	13(4)-12(4)	7.17	189	1.03(0.33)	0.33(0.08)
CH <sub>3</sub> CCH	13(5)-12(5)	6.75	253	1.04(0.35)	0.21(0.08)

<sup>a</sup> Blend of CH<sub>3</sub>CN at 12(0)-11(0) and 12(1)-11(1).

<sup>b</sup> Blend of CH<sub>3</sub>CCH at 13(0)-12(0) and 13(1)-12(1).

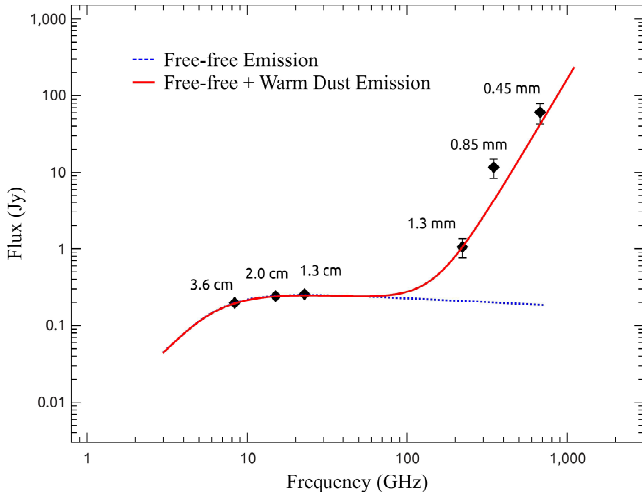


FIG. 12.— SED for HC H II G35.58-0.03 combining 3.6 cm, 2.0 cm, 1.3 cm, 1.3 mm, 0.85 mm, and 0.45 mm continuum data. The continuum total fluxes are listed in Table 2. The respective error bars were indicated in each data point. The dotted blue line is the SED fitting from free-free emission component, while the solid red line is the sum of the free-free emission and warm dust emission.

relation

$$N(^{13}\text{CO}) = 1.51 \times 10^{14} \text{cm}^{-2} \frac{e^{5.3/T_{\text{ex}}}}{1 - e^{-10.6/T_{\text{ex}}}} \int T_{\text{MB}} dv. \quad (14)$$

If we assume that the  $[\text{H}_2/^{13}\text{CO}]$  abundance ratio is  $8.9 \times 10^5$  (Garden et al. 1991), the molecular hydrogen column density,  $N(\text{H}_2)$ , can be calculated. The total mass of gas in the synthesized beam can be calculated from equation

$$M_{\text{out}} = 4.57 \times 10^{-19} M_{\odot} \left( \frac{\theta_{\text{beam}}}{\text{arcsec}} \right)^2 \left( \frac{N(^{13}\text{CO})}{\text{cm}^{-2}} \right) \left( \frac{D}{\text{kpc}} \right)^2, \quad (15)$$

where we assume that the mean atomic weight of the gas is  $\mu_g = 1.36$ ,  $\theta_{\text{beam}}$  is the synthesized beam size in arcsec, and  $D = 10.2$  kpc. The masses of blue and red lobes are 86 and 70  $M_{\odot}$ , respectively. The dynamical

timescale is  $t = 3 \times 10^4$  yr, and the total mass loss rate is  $\dot{M}_{\text{loss}} = 5.2 \times 10^{-3} M_{\odot} \text{yr}^{-1}$  from the equations in Goldsmith et al. (1984) and Qin et al. (2008). The mass loss rate  $\dot{M}_{\text{loss}}$  is less than the mass infall rate  $\dot{M}_{\text{in}}$ , so the infall is predominant, suggesting the envelope mass of central star is still increasing rapidly.

From the PV diagram in Figure 11, the outflow velocity with  $V_{\text{out}} \approx 10.0 \text{ km s}^{-1}$  was estimated relative to the systemic velocity  $V_{\text{sys}} \approx 52.5 \text{ km s}^{-1}$ . The momentum of the outflowing gas per year is  $\sim 0.052 M_{\odot} \text{ km s}^{-1}$  based on  $\dot{M}_{\text{loss}} = 5.2 \times 10^{-3} M_{\odot} \text{ yr}^{-1}$ . This value is very consistent with the momentum ( $\sim 0.050 M_{\odot} \text{ km s}^{-1}$ ) of the infalling gas per year. The momentum is conserved in the dynamical process of the HC H II region. The outflow movement can transfer the angular momentum of infalling materials, so that the mass of the central dense core will keep increasing.

#### 4.5.3. Rotation

The rotation axis is expected to be along the direction of the outflow, NE-SW. In Figure 9 for the intensity-weighted mean velocity (moment-1) maps of NH<sub>3</sub> (2, 2), there is also an obvious velocity gradient along the NW-SE direction in a small area, which is evidence for rotation. However, the velocity gradient direction is inverted for NH<sub>3</sub> (3, 3), possibly due to higher noise. We tried to find other evidence of rotation with the position-velocity diagram method of NH<sub>3</sub>, but failed. Higher resolution observations are necessary to unveil whether and how the rotation is precessing in HC H II region G35.58-0.03.

#### 4.6. Ammonia Absorption Lines

The metastable NH<sub>3</sub> (2, 2) and (3, 3) arise from energy levels of 65 K and 125 K, respectively; they usually trace very compact gas  $n(\text{H}_2) \sim 10^5 - 10^6 \text{ cm}^{-3}$  (Ho & Townes 1983; Churchwell 2002). Figure 4 presents the molecular spectral lines of NH<sub>3</sub> (2, 2) and (3, 3) with  $V_{\text{sys}} = 52.5 \text{ km s}^{-1}$  at the position of the 1.3 cm continuum peak. The velocity-integrated contours (Figure 8) of NH<sub>3</sub> (2, 2) and (3, 3) present a dense structure



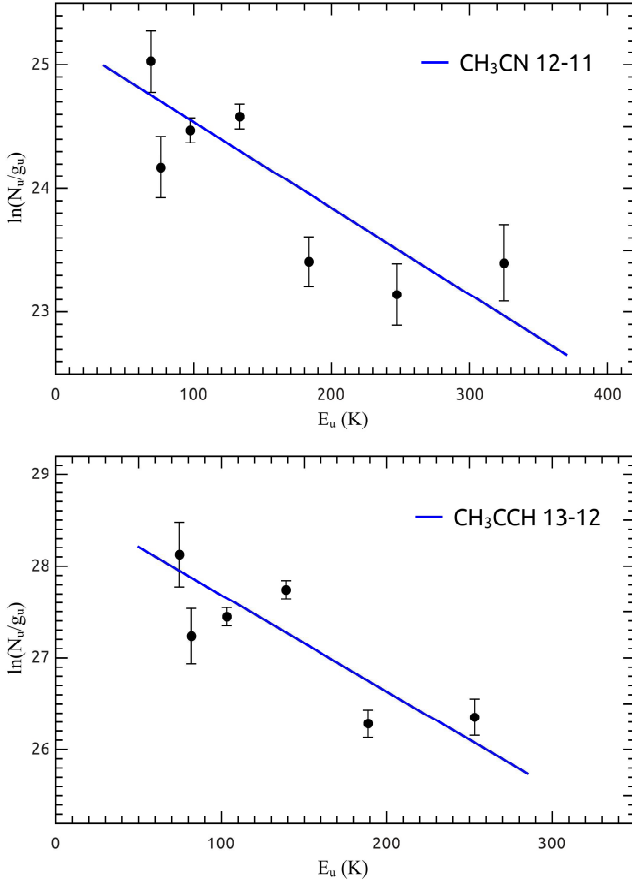


FIG. 13.— Rotational temperature diagrams for the  $\text{CH}_3\text{CN}$  and  $\text{CH}_3\text{CCH}$ . The filled circles with vertical error bars are for the observed transitions. The linear least-square fittings are shown as the solid blue line. The rotational temperatures derived from the diagram method are  $T_{\text{rot}} = 143 \pm 20$  K for  $\text{CH}_3\text{CN}$  and  $T_{\text{rot}} = 95 \pm 17$  K for  $\text{CH}_3\text{CCH}$ , respectively. The relevant parameters are listed in Table 3.

in front of the continuum with low velocity dispersion (Figure 10). The kinematic of the  $\text{NH}_3$  (2, 2) and (3, 3) lines is less obvious than that for the HC H II region G20.08-0.14N (Galván-Madrid et al. 2009), which shows evidence for accretion. The satellite hyperfine lines of  $\text{NH}_3$  (2, 2) and (3, 3) are very noisy. We just detect the ammonia absorption lines, but no emission lines.

To calculate the optical depth, excitation temperature, and column density of the molecular gas, we assume that the beam filling factors and the excitation temperatures are equal between the  $\text{NH}_3$  (2, 2) and (3, 3) main line, and in LTE. Figure 8 shows that the 1.3 cm continuum background almost covers the molecular gas distribution, so the apparent optical depth can be derived from the absorption depth (Keto et al. 1987)

$$\tau_{\text{app}} = -\ln\left(1 + \frac{S_{\text{NH}_3}}{S_{1.3\text{ cm}}}\right), \quad (16)$$

where  $S_{\text{NH}_3}$  and  $S_{1.3\text{ cm}}$  are estimated from the peak flux density of line and continuum. The apparent optical depths of  $\text{NH}_3$  main line are obtained with  $\tau_{\text{app}}(2, 2) = 0.65$  and  $\tau_{\text{app}}(3, 3) = 0.47$ .

Assuming  $h\nu \ll kT_{\text{ex}}$  and  $\tau(2, 2) = \tau_{\text{app}}(2, 2) = 0.65$ ,

the excitation temperature can be derived from equation (A17) in Mangum et al. (1992) with

$$T_{\text{ex}}(3, 3; 2, 2) = -59.1\text{K} \left\{ \ln \left[ \frac{0.847\Delta V(3, 3)}{\tau(2, 2)\Delta V(2, 2)} \times \ln \left( 1 - \frac{S_{\text{NH}_3}(3, 3)}{S_{\text{NH}_3}(2, 2)} (1 - e^{-\tau(2, 2)}) \right) \right] \right\}^{-1}, \quad (17)$$

where the  $\Delta V$  is the velocity width in  $\text{km s}^{-1}$ , and the  $S_{\text{NH}_3}$  is the line flux density. The excitation temperature of the  $\text{NH}_3$  main line is  $T_{\text{ex}}(3, 3; 2, 2) = 63 \pm 5$  K for the peak position. Then, the column density of  $N_{\text{NH}_3}(2, 2)$  (Mangum et al. 1992) is

$$N_{\text{NH}_3}(2, 2) = 3.11 \times 10^{14} \text{cm}^{-2} \frac{T_{\text{ex}}(2, 2)}{\nu(2, 2)} \tau(2, 2) \Delta V$$

where the  $\nu(2, 2)$  is the line frequency in GHz, and  $\Delta V$  is the velocity width in  $\text{km s}^{-1}$ . The resulting column density is  $N_{\text{NH}_3}(2, 2) = 2.5 \times 10^{15} \text{cm}^{-2}$ , and the abundance ratio between  $\text{NH}_3(2, 2)$  and  $\text{H}_2$  is  $[\text{NH}_3(2, 2)]/[\text{H}_2] = 10^{-7}$  (Ho & Townes 1983).

## 5. CONCLUSIONS

We have reported high angular resolution observations carried out with the SMA at 1.3 mm and the VLA at 1.3 cm toward the HC H II region G35.58-0.03. Combining spectral and continuum data, we have investigated the dynamical condition and morphological structure of the star formation region. The main results are summarized as follows.

1. With the 1.3 mm SMA and 1.3 cm VLA observations, we detected a total of 25 transitions of 8 different species and their isotopologues ( $\text{CO}$ ,  $\text{CH}_3\text{CN}$ ,  $\text{SO}_2$ ,  $\text{CH}_3\text{CCH}$ ,  $\text{OCS}$ ,  $\text{CS}$ ,  $\text{H}$ , and  $\text{NH}_3$ ). We presented the Gaussian fitting spectra, the moments 0, 1, and 2 maps, and continuum images. The systemic velocity  $V_{\text{sys}} \approx 52.5 \text{ km s}^{-1}$  was derived from the mean value of the velocities from Gaussian fits.
2. G35.58-0.03 is an HC H II core with electron temperature  $T_e^* = 5500 \text{ K}$ , emission measure  $\text{EM} \approx 1.9 \times 10^9 \text{ pc cm}^{-6}$ , local volume electron density  $n_e = 3.3 \times 10^5 \text{ cm}^{-3}$ , and broad radio recombination line emission with  $\text{FWHM} \approx 43.2 \text{ km s}^{-1}$ . The intrinsic core size is  $\sim 3714 \text{ AU}$ . We distinguish the free-free emission (25%  $\sim$  55%) from the warm dust component (75%  $\sim$  45%) at 1.3 mm continuum, from the continuum SED fitting among 3.6 cm, 2.0 cm, 1.3 cm, 1.3 mm, 0.85 mm, and 0.45 mm. An early-type star equivalent to an O6.5 star is postulated to have formed within the HC H II region based on the derived Lyman continuum photon number.
3. Both the  $\text{H}30\alpha$  and  $\text{H}38\beta$  lines have nearly the same  $\text{FWHM} \approx 43.2 \text{ km s}^{-1}$ . The observed line width  $\Delta V$  is due to the dynamical and/or turbulent movements of hot ionized gas with  $\Delta V_{\text{dyn}} \approx 40.1 \text{ km s}^{-1}$ , the thermal broadening contaminates  $\Delta V_{\text{ther}} \approx 15.87 \text{ km s}^{-1}$ , and the pressure

broadening only  $\Delta V_P \approx 0.02 \sim 0.06 \text{ km s}^{-1}$ . In addition, the H30 $\alpha$  line, probably participating in dynamical movements, shows evidence of blueshifted and redshifted wings. Therefore, H30 $\alpha$  shows evidence of an ionized outflow driving a molecular outflow.

4. The molecular envelope shows evidence of infall and outflow with an infall rate of  $0.033 \text{ M}_\odot \text{ yr}^{-1}$  and a mass loss rate of  $5.2 \times 10^{-3} \text{ M}_\odot \text{ yr}^{-1}$ , suggesting that the high accretion rate might have quenched the H II region inside. Both the momentum of the infalling and outflowing gas per year

are  $\sim 0.05 \text{ M}_\odot \text{ km s}^{-1}$ . A collimated bipolar outflow is detected in the moment-0 maps of CO (2-1),  $^{13}\text{CO}$  (2-1),  $^{13}\text{CS}$  (5-4), and SO $_2$  11(1,11)-10(0,10). The intensity-weighted mean velocity (moment-1) map of NH $_3$  (2, 2) has an obvious velocity gradient along the NW-SE direction, which is an indication for rotation.

We would like to thank the anonymous referee for her/his helpful suggestions and comments. We thank the SMA and VLA staff for making the observations possible.

## REFERENCES

- Anglada, G., Villuendas, E., Estalella, R., et al. 1998, *AJ*, 116, 2953
- Araya, E., Hofner, P., Kurtz, S., Bronfman, L., & DeDeo, S. 2005, *ApJS*, 157, 279
- Beuther, H., Leurini, S., Schilke, P., et al. 2007, *A&A*, 466, 1065
- Beuther, H., Zhang, Q., Greenhill, L. J., et al. 2004, *ApJ*, 616, L31
- Caswell, J. L., Vaile, R. A., Ellingsen, S. P., Whiteoak, J. B., & Norris, R. P. 1995, *MNRAS*, 272, 96
- Choi, M., Lee, J.-E., & Kang, M. 2012, *ApJ*, 747, 112
- Churchwell, E. 2002, *ARA&A*, 40, 27
- De Buizer, J. M., Radoski, J. T., Telesco, C. M., & Piña, R. K. 2005, *ApJS*, 156, 179
- Fish, V. L., Reid, M. J., Argon, A. L., & Zheng, X.-W. 2005, *ApJS*, 160, 220
- Fish, V. L., Reid, M. J., Wilner, D. J., & Churchwell, E. 2003, *ApJ*, 587, 701
- Forster, J. R. & Caswell, J. L. 1989, *A&A*, 213, 339
- Franco, J., Kurtz, S., Hofner, P., et al. 2000, *ApJ*, 542, L143
- Galván-Madrid, R., Keto, E., Zhang, Q., et al. 2009, *ApJ*, 706, 1036
- Garden, R. P., Hayashi, M., Hasegawa, T., Gatley, I., & Kaifu, N. 1991, *ApJ*, 374, 540
- Goldsmith, P. F. & Langer, W. D. 1999, *ApJ*, 517, 209
- Goldsmith, P. F., Snell, R. L., Hemeon-Heyer, M., & Langer, W. D. 1984, *ApJ*, 286, 599
- Gordon, M. A. & Sorochenko, R. L., eds. 2002, *Astrophysics and Space Science Library*, Vol. 282, Radio Recombination Lines. Their Physics and Astronomical Applications
- Ho, P. T. P., Moran, J. M., & Lo, K. Y. 2004, *ApJ*, 616, L1
- Ho, P. T. P. & Townes, C. H. 1983, *ARA&A*, 21, 239
- Keto, E. 2002, *ApJ*, 580, 980
- Keto, E. 2007, *ApJ*, 666, 976
- Keto, E., Zhang, Q., & Kurtz, S. 2008, *ApJ*, 672, 423
- Keto, E. R., Ho, P. T. P., & Haschick, A. D. 1987, *ApJ*, 318, 712
- Klaassen, P. D., Galván-Madrid, R., Peters, T., Longmore, S. N., & Maercker, M. 2013, *A&A*, 556, A107
- Kurtz, S. 2005, in *IAU Symposium*, Vol. 227, Massive Star Birth: A Crossroads of Astrophysics, ed. R. Cesaroni, M. Felli, E. Churchwell, & M. Walmsley, 111–119
- Kurtz, S., Churchwell, E., & Wood, D. O. S. 1994, *ApJS*, 91, 659
- Kurtz, S. E. 2000, in *Revista Mexicana de Astronomía y Astrofísica*, vol. 27, Vol. 9, Revista Mexicana de Astronomía y Astrofísica Conference Series, ed. S. J. Arthur, N. S. Brickhouse, & J. Franco, 169–176
- Kurtz, S. E., Watson, A. M., Hofner, P., & Otte, B. 1999, *ApJ*, 514, 232
- Lang, K. R. 1980, *Astrophysical Formulae. A Compendium for the Physicist and Astrophysicist*.
- Lis, D. C., Carlstrom, J. E., & Keene, J. 1991, *ApJ*, 380, 429
- Mangum, J. G., Wootten, A., & Mundy, L. G. 1992, *ApJ*, 388, 467
- Matsakis, D. N., Evans, II, N. J., Sato, T., & Zuckerman, B. 1976, *AJ*, 81, 172
- Mehring, D. M. 1994, *ApJS*, 91, 713
- Mezger, P. G. & Henderson, A. P. 1967, *ApJ*, 147, 471
- Mezger, P. G., Smith, L. F., & Churchwell, E. 1974, *A&A*, 32, 269
- Mueller, K. E., Shirley, Y. L., Evans, II, N. J., & Jacobson, H. R. 2002, *ApJS*, 143, 469
- Müller, H. S. P., Schlöder, F., Stutzki, J., & Winnewisser, G. 2005, *Journal of Molecular Structure*, 742, 215
- Myers, P. C., Linke, R. A., & Benson, P. J. 1983, *ApJ*, 264, 517
- Panagia, N. 1973, *AJ*, 78, 929
- Pickett, H. M., Poynter, R. L., Cohen, E. A., et al. 1998, *J. Quant. Spec. Radiat. Transf.*, 60, 883
- Plume, R., Jaffe, D. T., & Evans, II, N. J. 1992, *ApJS*, 78, 505
- Qin, S.-L., Wang, J.-J., Zhao, G., Miller, M., & Zhao, J.-H. 2008, *A&A*, 484, 361
- Qin, S.-L., Wu, Y., Huang, M., et al. 2010, *ApJ*, 711, 399
- Reynolds, S. P. 1986, *ApJ*, 304, 713
- Rubin, R. H. 1968, *ApJ*, 154, 391
- Sewilo, M., Churchwell, E., Kurtz, S., Goss, W. M., & Hofner, P. 2011, *ApJS*, 194, 44
- Shi, H., Zhao, J.-H., & Han, J. L. 2010, *ApJ*, 710, 843
- Shirley, Y. L., Evans, II, N. J., Young, K. E., Knez, C., & Jaffe, D. T. 2003, *ApJS*, 149, 375
- Snell, R. L., Scoville, N. Z., Sanders, D. B., & Erickson, N. R. 1984, *ApJ*, 284, 176
- van der Tak, F. F. S. & Menten, K. M. 2005, *A&A*, 437, 947
- Walmsley, M. 1995, in *Revista Mexicana de Astronomía y Astrofísica Conference Series*, Vol. 1, Revista Mexicana de Astronomía y Astrofísica Conference Series, ed. S. Lizano & J. M. Torrelles, 137
- Watson, C., Araya, E., Sewilo, M., et al. 2003, *ApJ*, 587, 714
- Wilson, T. L., Rohlfs, K., & Hüttemeister, S. 2009, *Tools of Radio Astronomy* (Springer-Verlag)
- Wong, T., Ladd, E. F., Brisbin, D., et al. 2008, *MNRAS*, 386, 1069
- Zhang, C.-P. & Wang, J.-J. 2013, *Research in Astronomy and Astrophysics*, 13, 47